Ph.D. DISSERTATION

Control of Fano Resonance in Plasmonic and Optical Systems for Highly-Sensitive Spectral Responses

플라즈모닉 및 광학 시스템에서의 스펙트럼 민감도 향상을 위한 파노 공명의 제어

By

Xianji Piao

AUGUST 2015

DEPARTMENT OF ELECTRICAL ENGINEERING AND
COMPUTER SCIENCE
COLLEGE OF ENGINEERING
SEOUL NATIONAL UNIVERSITY

Abstract

Control of Fano Resonance in Plasmonic and Optical Systems for Highly-Sensitive Spectral Responses

Xianji Piao

DEPARTMENT OF ELECTRICAL ENGINEERING AND COMPUTER SCIENCE

COLLEGE OF ENGINEERING

SEOUL NATIONAL UNIVERSITY

The concept of Fano resonance from quantum physics has originally been applied to describe the configuration interaction in the rare gas excitation, which is one of the universal phenomena caused by the wave interference. The main feature of Fano resonance is the sharp, asymmetrically shaped spectrum, which is due to the interference between two resonant modes of different life-time. To exploit this intriguing spectral feature, a variety of Fano resonant nanostructures implementing optical analogue of quantum-mechanical Fano resonance have been proposed and studied, including

clusters of plasmonic nanoparticles and metamaterial platforms. During my Ph.D study I have been trying to bring the concept of Fano resonance into the field of optical and plasmonic systems to provide some novel paths for the existing applications such as on-chip plasmonic devices and net optical spin excitation. In this dissertation, the characteristics of asymmetrically shaped spectral responses for the Fano resonant structures are investigated in the plasmonic stub-waveguide systems and optical chiral system.

In the theoretical part of this dissertation, the theoretical descriptions about the Fano resonance phenomena are provided in several different formalism, such as the original quantum perturbation analysis, analogy with classical oscillators, and the simple and general coupled mode theory. Based on the coupled mode theory model, I also establish the Fano asymmetry parameter, which is the key physical parameter for the quantification of the Fano resonance phenomenon.

Through the numerical and theoretical studies, we firstly propose a plasmonic sensor based on the control of the degree of Fano asymmetry, with the plasmonic metal-insulator-metal waveguide-stub junction structure. we also introduce an ultra-efficient plasmonic on-chip modulator based on the concept of plasmonic induced transparency. Excellent performance

with 12dB transmission contrast at ~60% throughput is achieved due to the extremely sharp spectral profiles, which is caused by the Fano interference using a pair of plasmonic metal-insulator-metal stubs. A novel path for the conservative and nonmagnetic optical spin excitation is introduced utilizing the spin handedness-dependent anti-symmetric Fano resonances, with Hermitian material parameters. Utilizing the pure optical spin excitation density and its extreme spectral sensitivity in the suggested design, ‘optical spin switching’ is also introduced with experimentally accessible material parameters.

Keywords: Fano resonance, Optics, Plasmonics, Plasmon-induced transparency, Chirality,

Student Number: 2008-23515

Contents

List of Figures

Chapter 1

Introduction

1.1 Motivation

Fano resonance is originally used to describe the ionization spectra of atoms and molecures in quantum physics [1, 2]. It is the representative phenomena based on the notion of electron wavefunction not on its density, because phase information plays a critical role in Fano-type interactions: resulting in asymmetric spectral line shapes in scattering profiles. Due to its motivating spectral feature which opens a pathway to the drastic response beyond its natural quality factor, Fano spectral asymmetry has also been studied intensively in optics, in terms of the interactions between broadband and

narrowband optical elements [3-5]. Many guided-wave devices, metamaterials and beam dynamics showing various types of Fano resonances have been suggested and demonstrated [3-15].

In this dissertation, I will discuss the intriguing properties of several plasmonic and optical systems, as well as their potential contribution to some of the novel applications. For example, our research in plasmonic interference between the waveguide mode and local mode shows the potential of sharp spectral response based on proper geometrical optimization [16], while the link to the electromagnetically induced transparency provides ultra-sensitive plasmonic on-chip modulator [17], and antisymmetric Fano resonance induced spectral separation of photon with different handedness provides conservative and nonmagnetic paths for the control of optical spin angular momentum.

1.2 Fano Resonance in the Spectral Domain

1.2.1 Asymmetrically shaped spectrum

The asymmetrically shaped spectrum is one of the most intriguing features of Fano resonance, which is the result of the destructive interference between the direct and indirect excitation of the bound state [3-5]. Fano interference is one of the most important quantum interferences, which occurs between

discrete and continuum states. The simplest analogy of Fano system with optical resonators and waveguide is shown in Fig. 1.1a [17], where the Fano resonance is the result of the interference between the narrowband (ψ_1) and broadband mode (ψ_0). (Fig. 1.1b [4]).

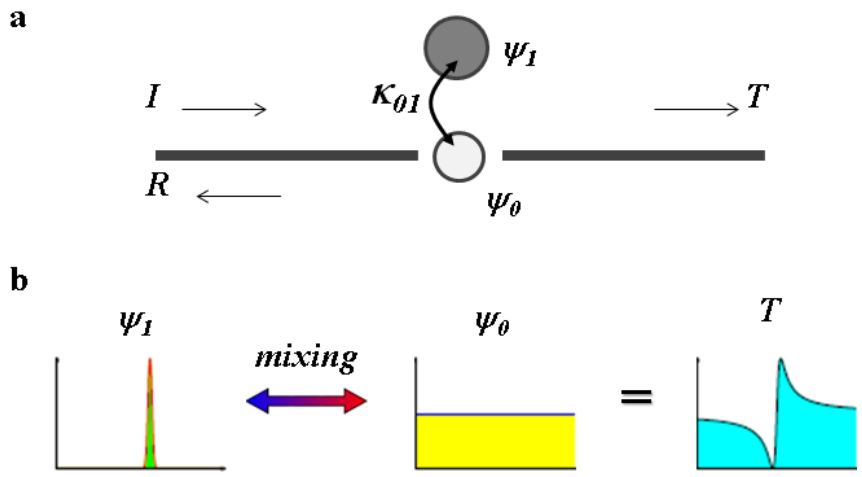

Figure 1.1 (a) Schematics of the Fano resonance [17] described as the mixing between a discrete state (side-coupled narrowband resonator, ψ_1) and a continuum waveguide state (a broadband resonator, ψ_0). (b) A simple model of the Fano resonant system with bright (ψ_0) and dark resonant mode (ψ_1) [4]. .

1.2.2 Fano Asymmetry Parameter

In the original paper [1, 2], Fano explained the asymmetrically shaped

scattering spectra with a perturbation approach. To address the Fano resonance quantitatively, Fano introduced a parameter q as the ratio of the transition probabilities to the mixed resonant state and to the continuum [1, 4].

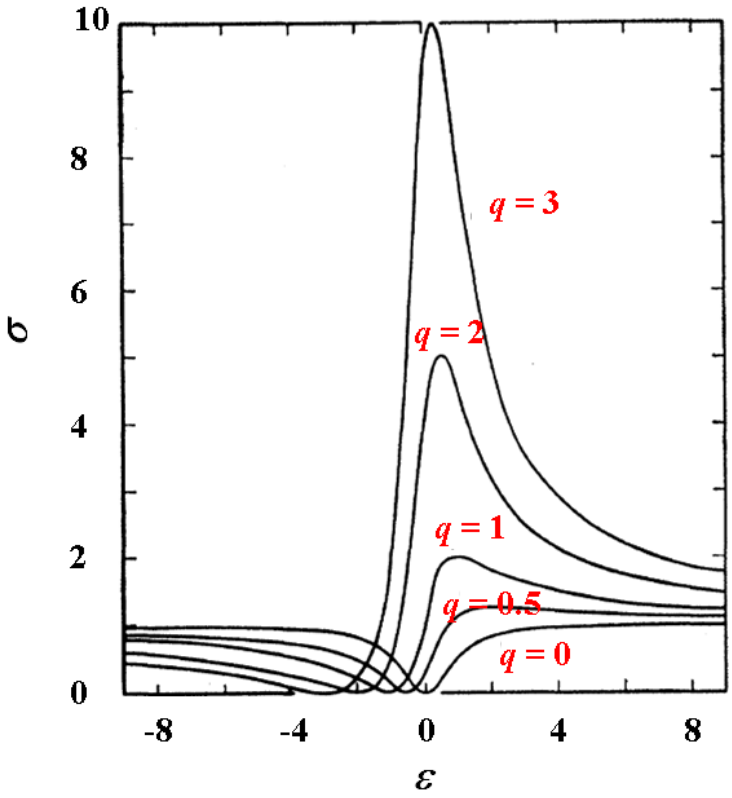

Figure 1.2 Natural line shapes with different degree of asymmetry for different values of q [1].

As a result, Fano obtained the formula for the shape of a scattering cross

section [1]:

$$\sigma = \frac{(\varepsilon + q)^2}{\varepsilon^2 + 1} \tag{1.1}$$

where q is a phenomenological shape parameter, and ε represents reduced energy, defined as $2(E - E_F) / \Gamma$, with the resonant energy E_F and bandwidth Γ. As can be seen in Fig. 1.2, with the increase of the q, the strength of the spectral asymmetry is getting stronger. The spectral line shapes becomes symmetry when the amplitude of q approaches 0 or infinite.

1.3 Fano Resonance in the Spatial Domain

1.3.1 Introduction of Goos-Hanchen shift

In 1947, Goos and Hanchen firstly observed the spatial lateral shift of the center of the incident beam with linear polarization, when it is totally reflected from a dielectric surface [18-22]. The reason for the spatial displacement is predicted by the geometric optics that each plane-wave components of incident beam undergoes a different phase change [18-22]. This effect (called Goos-Hanchen effect) has been intensively studied theoretically and experimentally [18, 19], and usually known to be much smaller than the beam width [19].

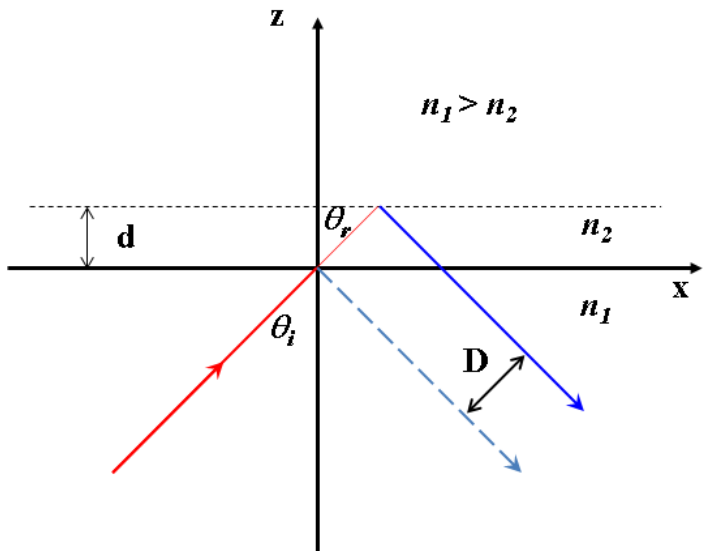

Figure 1.3 Schematics of the Goos-Hanchen effect (lateral shift D) with the estimation of the existence of the evanescent wave (skin depth d) at the interface of two media ($n_1 > n_2$).

However, in nanophotonic devices the beams are considerably small, Goos-Hanchen effect should be taken into account. As shown in Fig. 1.3 [18], the penetration of the evanescent wave into the region of smaller index refraction ($n_1 > n_2$). Under the rough estimation the lateral shift can be written as $D \approx 2d \cdot \sin\theta_i$. where θ_i is the incident angle. The skin depth is $d^{-1} = k \cdot (\sin^2\theta_i - \sin^2\theta_c)$, where k is the wave vector, and $\theta_c = \sin^{-1}(n_2 / n_1)$ is the critical angle.

1.3.2 Giant Goos-Hanchen shift with Fano Resonance

Recently, several studies suggested that larger lateral shifts of beam can be achieved through the excitation of surface states [18-22]. According to Artmann [18], the relation between the Goos-Hanchen shift (D) and the phase (φ) of complex reflection coefficient can have the following relationship:

$$D = -\frac{\lambda}{2\pi}\frac{\partial\varphi(\theta_i)}{\partial\theta_i}. \tag{1.2}$$

Equation 1.2 shows that to increase the value of D a larger derivative of the phase for the reflectance angular resonance is required. In other words, a narrower resonance leads to the larger Goos-Hanchen shift. Since Fano interference also caused by the phase change induced by the narrowband state, it can be indirectly related to the Goos-Hanchen effect through the excitation of surface wave state. Considering the phase-matching condition between the incident field and surface wave, a surface-polariton can be applied in a layered structure. Therefore, a significant increase of the lateral displacement has been achieved by the excitation of surface plasmons [19-21] or Bloch waves in photonic crystals [18, 22]. As shown in Fig. 1.4 [18], with the excitation of the Bloch surface wave at 532 nm wavelength, a greatly enhanced Goos-Hanchen shift is achieved (~125 λ).

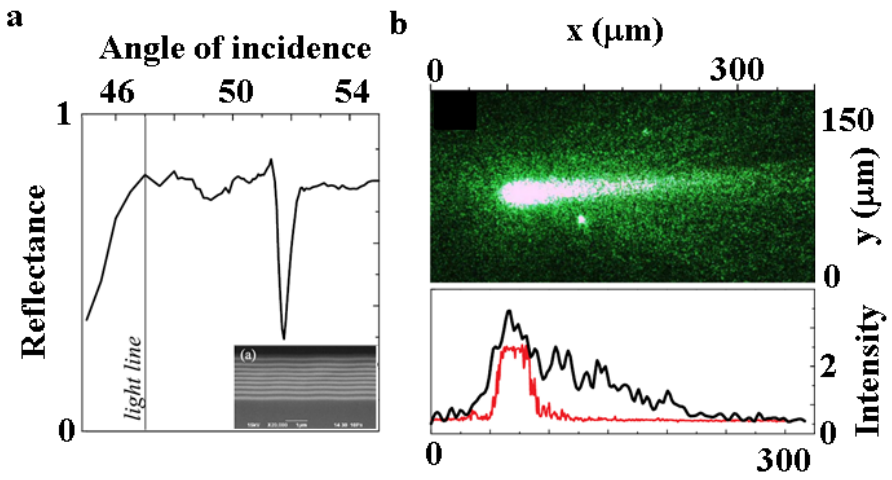

Figure 1.4 (a) Reflectance angular spectrum of a 1D photonic crystal (inset) for s-polarized incident light. (Dip at 52° indicates surface wave excitation). (b) Microimage (up) and line profiles of intensity (down, red: s-polarized, black: p-polarized) of the surface wave [18].

1.4 Optical Fano Resonance in the Temporal Domain

In this section I will discuss universal temporal phase formalism [15], which can be applied to mapping the Fano asymmetry parameter q to a phase $\varphi(t)$ of temporal dipole response. As shown in Fig. 1.5 [15], the reason of the Fano spectral asymmetry can be understood to be the temporal phase shift φ_{Fano}, compared to the Lorentzian case with symmetric line shape.

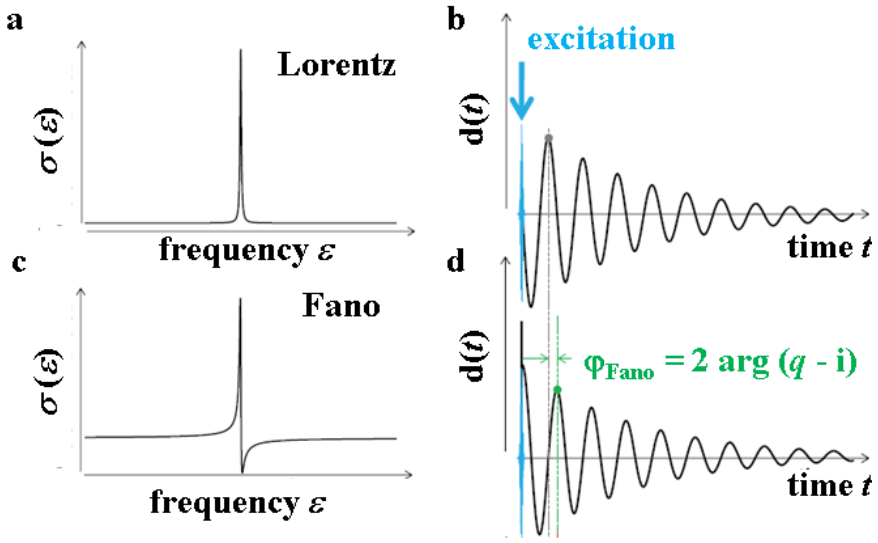

Figure 1.5 (a) Spectral absorption response with Lorentz symmetric line shape. (b) Lorenzian temporal dipole response function, with the well-known exponential decay. (c) Fano asymmetric spectral line shape. (d) Fano temporal dipole response function, having a phase shift φ_{Fano} compared to the Lorentzian case [15].

Christian Ott [15] introduced the following expression for the link between spectral Fano asymmetry and temporal phase shift:

$$\varphi(q) = 2\arg(q - i)\ , \tag{1.3}$$

and in turn we can have,

$$q(\varphi) = i\left|\frac{1+\exp(i\varphi)}{1-\exp(i\varphi)}\right| . \qquad (1.4)$$

Equation 1.3 and 1.4 [15] indicate that when $\varphi = 0$, the function of Lorentzian dipole response can be obtained (Fig. 1.5b).

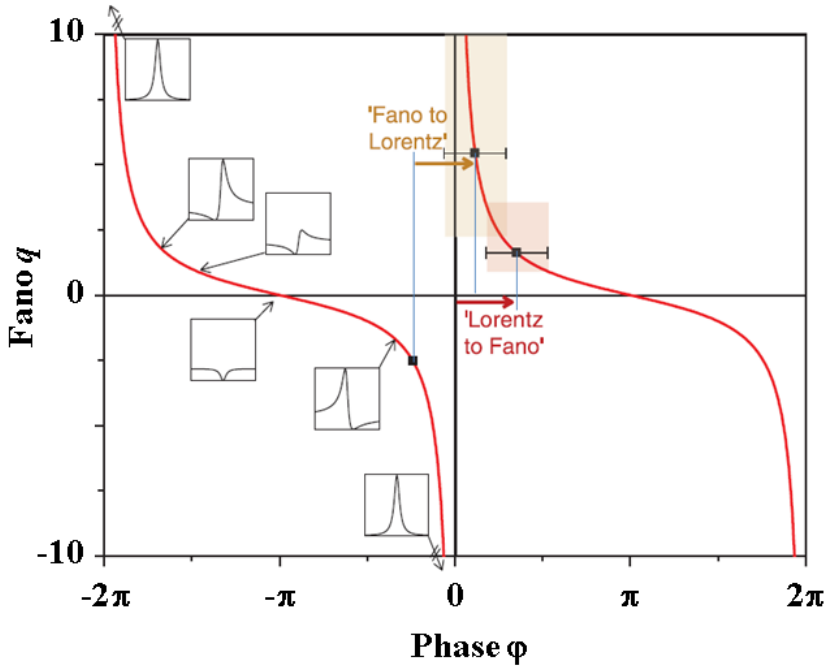

Figure 1.6 Mapping of Fano asymmetry parameter q to the temporal phase φ. Insets show the spectral line shapes σ (ε) for the selected value of q (φ) [15]

Based on this formalism the asymmetric Fano line shape can be

quantified in the time domain. This formalism can be applied to the control or the transforming of spectral responses, e.g., by applying temporally delated laser excitation, the spectral responses can be transformed from symmetric Lorentz resonance to asymmetric Fano resonance, or from asymmetric to symmetric resonance.

1.5 Achievements and Challenges

As the physical origin and critical parameters of Fano effects have been identified in ordinary platforms, recent studies have been focused on Fano resonances for distinctive physical quantities or for the link with other physical phenomena: such as the interaction between electric and magnetic dipoles [14] (Fig. 1.7a), Fano resonance with polarization preference [13] (Fig. 1.7b), and electronic observation of optical Fano resonance [12] (Fig. 1.7c).

Similar to these tendencies, here we investigate Fano resonance linked with plasmonic local mode with MIM T-junction structure (chapter 3 [16]), electromagnetically induced transparency (chapter 4 [17]), and Fano-resonant induced optical spin angular momentum (chapter 5).

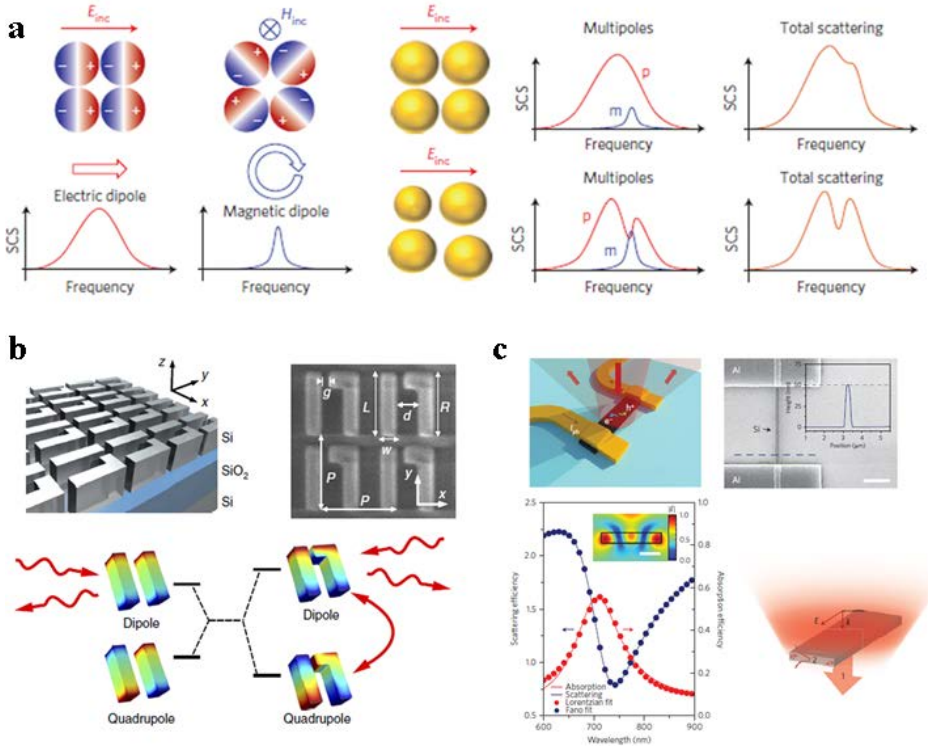

Figure 1.7 The examples of Fano resonances in optics: (a) the interaction between electric and magnetic dipoles [14], (b) the interaction with chiral optical elements [13], and (c) the electronic observation of optical Fano resonances [12].

1.6 Dissertation Overview

Fano resonance is a widely existed phenomenon, which offers a unique path to the study of phase interference effect and the associated electromagnetic phenomena. This dissertation represents such a study for optical and

plasmonic systems, including “spectral asymmetry control using plasmonic metal-insulator-metal waveguide-stub structure”, “plasmon-induced transparency with metal-insulator-metal stub pair”, and “Antisymmetric Fano induced optical spin angular momentum”.

Chapter 2 provides the existing theoretical modeling methods for the description of the Fano resonance [1, 2], including the classical oscillator model, and coupled mode theory.

In chapter 3 [16], analytical and numerical studies of Fano interference, which occurs between the local plasmon mode and the stub mode is investigated analytically and numerically. By deriving the Fano asymmetry parameter analytically based on the coupled mode theory modeling, we unveil the geometric parameters which affect the spectral responses of the plasmonic stub-waveguide system.

Chapter 4 provides studies about the electromagnetically induced transparency, originally from the 4-level system in quantum mechanics, and provides plasmonic analogue of this phenomenon with metal-insulator-metal waveguide-stub platform [17]. We show the existence of Fano asymmetry in the transparency analytically and numerically. A plasmonic waveguide based on-chip modulator is demonstrated numerically with greatly enhanced performance.

In chapter 5, the phenomenon of optical spin dependent Fano resonance is studied and the excitation of optical spin angular momentum is demonstrated. The origin of the spin-dependent Fano resonance is unveiled based on the temporal response of the optical chiral resonator, which is the projection of the counter-rotated spin eigenvectors in the polarization space.

Finally, the work covered in this dissertation is summarized in chapter 6.

Chapter 2

Theoretical Model for the Fano Resonance

2.1 Introduction

Subsequent to Fano's paper, asymmetrically shaped resonances have been observed in various systems, such as plasmonic nanostructures and metamateirlas, and therefore becomes the key element of the optics.

In this chapter, I will introduce a general theoretic model based on temporal coupled mode theory, which can be used to describe a Fano resonance. Before proceeding to any specific descriptions of coupled mode theory, firstly I will discuss the original quantum perturbation analysis [1, 2],

and classical oscillator analogy for the Fano resonance for the rare gas excitations. Then the analogy of Fano resonance with the motion equation of coupled classical oscillators will be discussed for the intuitive interpretation [4, 23, 24]. Finally I will introduce the simple general formalism of coupled mode theory [4, 25-32], which will be the main modeling tool for the Fano resonant systems in the following chapters.

2.2 The Original Fano Approach

In 1935, Ugo Fano pointed out the asymmetric peaks with rare gas spectra, and provided theoretical interpretation of the origin of this asymmetry, which is the mixed configuration of autoionized levels with continuous absorption spectra. In 1961, he provided an extended and improved theory and reformulation for the same phenomenon, which bought out the connection with the theory of resonant scattering [16].

In this section I will discuss the reformulation of the original Fano approach [1, 2], for the simplest case of 'one discrete state and one continuum'. Consider among the states of an atomic system, there are states belonging to a discrete configuration φ and a continuum of states $\psi_{E'}$. With all the degeneracy having been removed, the energy matrix will be indicated as follows [1]:

$$\langle \varphi | H | \varphi \rangle = E_{\varphi} \tag{2.1}$$

$$\langle \psi_{E'} | H | \varphi \rangle = V_{E'} \tag{2.2}$$

where these matrices belong to the limited subsets of states $\psi_{E'}$, and the discrete energy level E_{φ} lies within the range of E'. The corresponding eigenvector Ψ_E has the form [1]

$$\Psi_E = a\varphi + \int dE' b_{E'} \psi_{E'} \quad , \tag{2.3}$$

where the coefficients a and $b_{E'}$ are the functions of eigenvalue E, which is an energy value within the range of E'. Then, these coefficients are the solutions of equations:

$$E_{\varphi} a + \int dE' V_{E'}^{*} b_{E'} = Ea \quad , \tag{2.4}$$

$$V_{E'} a + E' b_{E'} = E b_{E'} \quad . \tag{2.5}$$

The solution can write as [1]:

$$a = \frac{\sin \Delta}{\pi V_E} \quad , \tag{2.6}$$

$$b = \frac{V_{E'}}{\pi V_E}\frac{\sin\Delta}{E-E'} - \cos\Delta\cdot\delta(E-E') \quad , \tag{2.7}$$

where Δ = - *arctan*[$\pi|V_E|^2$ / (E - E_φ - $F(E)$)] represents a phase shift due to the interaction of discrete and continuum state. Here $F(E)$ = $P(\int dE' \, |V_{E'}|^2 / (E-E')$) and '*P*' indicates 'principle part of'.

The purpose of this section is to study the probability of excitation of the final stationary state Ψ_E, and with suitable transition operator T between the initial state i, and also from Eq. (2.3), (2.6) and (2.7) we have [1]

$$\left\langle \Psi_E \middle| T \middle| i \right\rangle = \frac{1}{\pi V_E^*}\left\langle \Phi \middle| T \middle| i \right\rangle \sin\Delta - \left\langle \psi_E \middle| T \middle| i \right\rangle \cos\Delta \quad , \tag{2.8}$$

where $\Phi = \varphi + P(\int dE' \, V_{E'}\psi_{E'} / (E - E')$) indicates the modified discrete state φ by the continuum $\psi_{E'}$. The sharp change of phase term Δ as E passes through the resonance at $E = E_\varphi + F(E)$ leads to the sharp variation of $<\Psi_E|T|i>$. Furthermore, since cosΔ is an odd function of (E - E_φ - $F(E)$), while sinΔ is an even function, the contribution from $<\Phi|T|\, i>$ and $<\psi_E|T|\, i>$ interfere with opposite phase on the each side of resonance.

Finally the curves of the ratio of the transition probabilities can be represented by

$$\sigma = \frac{\left|\left\langle \Psi_E \middle| T \middle| i \right\rangle\right|^2}{\left|\left\langle \psi_E \middle| T \middle| i \right\rangle\right|^2} = \frac{(q+\varepsilon)^2}{1+\varepsilon^2} \quad , \tag{2.9}$$

where $\varepsilon = (E - E_\varphi - F(E)) / (\pi|V_E|^2)$ is the reduced energy variable, and $q = (<\Phi|T|\, i>) / (\pi V_E^* <\psi_E|T|\, i>)$ [1].

2.3 Modeling with Classical Oscillators

Since the configuration interaction does not depend on the matter, Fano resonance can be considered as a universal phenomenon, which occurs due to the interference of waves from different channels. Therefore, to provide an intuitive description of Fano resonance and its asymmetry parameter q, in this section I would like to provide the theoretical model based on the analogy with coupled oscillators (Fig. 2.1) [4, 23, 24].

Recall the equations of motion for a single oscillator, which is under the influence of linear restoring force, a resisting force, and an external driving force (as shown in Fig. 2.1a), we can write the differential equations for the coupled oscillators as follows:

$$\begin{aligned} &\ddot{x}_1 + \gamma_1 \dot{x}_1 + \omega_1^2 x_1 + \nu_{12} x_2 = a_1 e^{i\omega t} \\ &\ddot{x}_2 + \gamma_2 \dot{x}_2 + \omega_2^2 x_2 + \nu_{12} x_1 = 0 \end{aligned} \quad , \tag{2.10}$$

where ω_1 (or ω_2) is the natural frequency of each oscillator without damping, γ_1 (or γ_2) is the frictional parameter, v_{12} is coupling coefficient, and ω and a_1 is the frequency and amplitude of the external driving force (Fig. 2.1a). Under the weak coupling estimation (ω_2^2 - ω_1^2 >> v_{12}), the eigenmodes of coupled system will have slightly shifted resonances from the one of independent oscillators, which can be written as:

$$\tilde{\omega}_1^2 \approx \omega_1^2 - \frac{v_{12}^2}{\omega_2^2 - \omega_1^2} \quad , \quad \tilde{\omega}_2^2 \approx \omega_2^2 + \frac{v_{12}^2}{\omega_2^2 - \omega_1^2} . \tag{2.11}$$

The general steady state solutions can be expressed in the harmonic complex form as $x_1 = c_1 \exp(i\omega t)$, and $x_2 = c_2 \exp(i\omega t)$. Then, the amplitudes can be written as follows [23, 24]:

$$\begin{aligned} c_1 &= \frac{(\omega_2^2 - \omega^2 + i\gamma_2\omega)}{(\omega_1^2 - \omega^2 + i\gamma_1\omega)(\omega_2^2 - \omega^2 + i\gamma_2\omega) - v_{12}^2} a_1 \\ c_2 &= \frac{v_{12}}{(\omega_1^2 - \omega^2 + i\gamma_1\omega)(\omega_2^2 - \omega^2 + i\gamma_2\omega) - v_{12}^2} a_1 \end{aligned} \quad , \tag{2.12}$$

In Fig. 2.1b a shifted resonance at $\tilde{\omega}_2 = 1.21$ with asymmetric profile can be observed compared to the symmetric one presented in Fig. 2.1d. The reason for the asymmetric peak in Fig. 1b is the existence of the $\omega_2 = 1.2$, which is close to the peak position. Meanwhile, as shown in Fig. 1d, since

the zero frequency of the first oscillator (at ω_1 = 1.0) is far from the peak position of the second oscillator the interaction term has much smaller influence. Then the phase of the oscillators can be defined as:

$$c_1(\omega) = |c_1(\omega)| e^{-i\varphi_1(\omega)} \ , \ \ c_2(\omega) = |c_2(\omega)| e^{-i\varphi_2(\omega)} . \qquad (2.13)$$

As shown in Fig. 2.1c and Fig. 2.1e, the phases of both oscillators undergo a π jump abruptly when the frequency of driving force crosses the resonances. However, there exists phase difference after the frequency of the driving force passing through the anti-resonance point at ω = 1.2. Because the phase of the first oscillator drops abruptly by π at the anti-resonance point, while the second oscillator experiences π phase gain. Then the two oscillators are eventually out of phase at the special position.

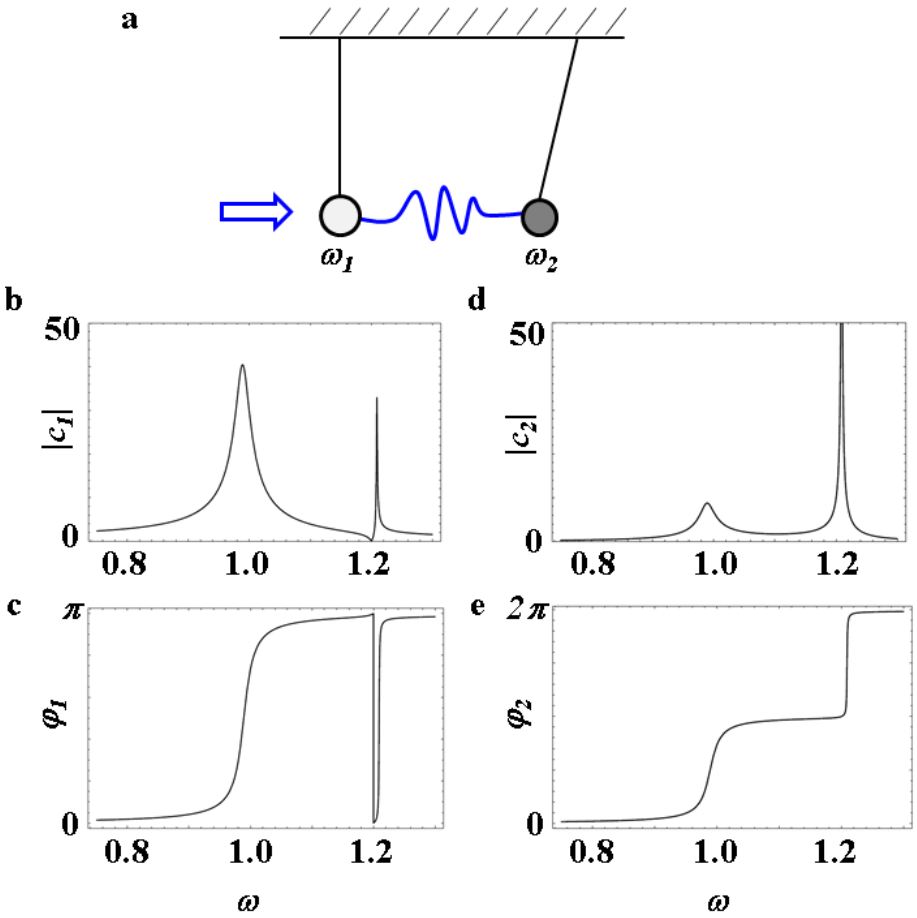

Figure 2.1 (a) Schematic diagram of two oscillators coupled by a weak spring [4]. Driving force (blue arrow) applied to one of the oscillators. (b, c) Amplitude ($|c_1|$) and phase (φ_1) behavior of first oscillator (ω_1); also, (d, e) amplitude ($|c_2|$) and phase (φ_2) for the second oscillator (ω_2) around the resonances [23].

2.4 Modeling with Coupled Mode Theory

2.4.1 Why Coupled mode formalism

In previous section, a spring mass model is provided for the Fano resonance, and its basic equation is a second-order differential equation. In this section I will introduce the coupling of modes formalism with first-order differential equation, which is based on few physical concepts and minimum of algebra [27]. Using the coupled mode theory, having the essential parameters only, one can focus on the coupling of a resonator to another, or one or more waveguide modes, based on perturbation analysis.

2.4.2 Basic theory of coupled mode theory

In this section I will introduce the coupling of modes formalism, and some details about the development. Here we can start from a simple *LC* circuit (Fig. 2.2) to understand the meaning amplitude of resonance (*a*).

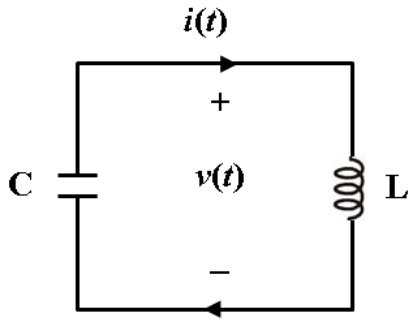

Figure 2.2 An LC circuit

The equations of the LC circuit are

$$v = L\frac{di}{dt}\ ,\ i = -C\frac{dv}{dt}\ . \tag{2.14}$$

These two coupled first-order differential equations lead to the second order differential equation for the voltage $v(t)$ as follows,

$$\frac{d^2v}{dt^2} + \omega_0^2 v = 0\ , \tag{2.15}$$

where $\omega_0 = (LC)^{1/2}$. By defining a complex variable [27]

$$a_{\pm} = \sqrt{\frac{C}{2}}\left(v \pm j\sqrt{\frac{L}{C}}\,i\right)\ , \tag{2.16}$$

we obtain a couple of complex conjugated first-order differential equations which can independently describe the resonance [27].

$$\frac{da_{\pm}}{dt} = \pm j\omega_0 a_{\pm} \quad , \tag{2.17}$$

For the better understanding of the meaning of *a*, we consider the solutions to the Eg. (2.14),

$$\begin{aligned} v(t) &= |V| \cos(\omega_0 t + \phi) \\ i(t) &= \sqrt{\frac{C}{L}} |V| \sin(\omega_0 t + \phi) \end{aligned} \quad , \tag{2.18}$$

where $|V|$ is the maximum of voltage and ϕ is the phase. Therefore,

$$a_{+} = \sqrt{\frac{C}{2}} V \exp(j\omega_0 t) \quad , \tag{2.19}$$

where a_+ has the dependence $\exp(j\omega_0 t)$, and then it can be normalized as

$$|a_{+}|^2 = \frac{C}{2}|V|^2 = W \quad . \tag{2.20}$$

where W is the energy of the circuit, and a_+ is the positive frequency component of the mode amplitude.

Now considering the case with an incident wave as shown in Fig. 2.3,

we have to include the modified decay rate of the resonator and the excitation amplitude of the resonant mode by the incidence. Here the excitation rate is indicated by a coupling coefficient κ, which represents the coupling strength between the resonant mode and the waveguide mode.

Figure 2.3 Schematics of the coupled resonator-waveguide system based on the coupling of modes formalism.

Here s_+ indicates the amplitude of the incident wave, which is normalized so that the power carried by the incident wave equals to $|s_+|^2$. In contrast to $|s_+|^2$, $|a|^2$ is normalized to the energy.

$$\frac{da}{dt} = j\omega_0 a - \left(\frac{1}{\tau_0} + \frac{1}{\tau_e}\right)a + \kappa \cdot s_+ \quad , \tag{2.21}$$

where τ_0 indicates the life time of the resonant mode only, which is related to the internal energy dissipation, and τ_e indicates the external dissipation such

as waveguide. These dissipation parameters are defined by $dW / da = a^*(da / dt) + a(da^* / dt) = -2(1/\tau_0 + 1/\tau_e)W$. Equation (2.21) is the main equation of the coupled mode theory and it can be extended to the system (as shown in Fig. 2.4) consists of a single-mode resonator coupled with multiple waveguides [25-28, 32].

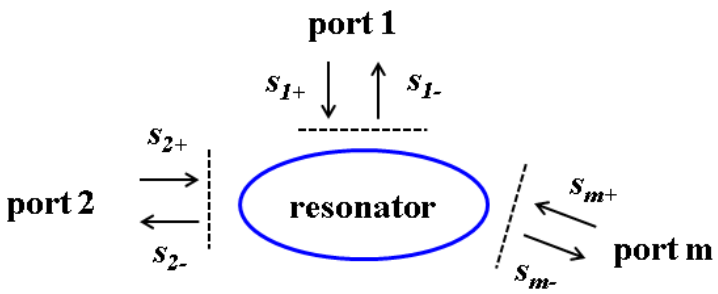

Figure 2.4 Schematics for the system consists of a single mode resonator coupled with multiple waveguides [26].

2.4.3 Coupled mode theory model for the Fano resonance

Based on the simple and general approach of coupled mode theory, we can directly predict the line-shape of the resonance system, e.g. the asymmetry in the Fano resonance and also the strength of the asymmetry. In this section I will show the observation of the Fano resonance based on the simplest coupled resonator-waveguide system which is presented in Fig. 1.1a.

$$\frac{da_0}{dt} = j\omega_0 a_0 - \frac{1}{\tau_0} a_0 + \kappa_{01} \cdot a_1 + \kappa_0 \cdot s_{in}$$
$$\frac{da_1}{dt} = j\omega_1 a_1 - \frac{1}{\tau_1} a_1 + \kappa_{01} \cdot a_0 \quad , \qquad (2.21)$$

where a_0 and ω_0 indicate the amplitude of the assumed broadband resonator (ψ_0), a_1 and ω_1 for the side-coupled narrowband resonator (ψ_1), κ_0 indicate the input and output waveguide port, and κ_{01} represent the coupling port to the side resonator. The amplitudes of scattering waves can be expressed as $s_r = \kappa_0^* a_0$ for the reflection, and $s_t = s_{in} + \kappa_0^* a_0$ for the transmission. Then the reflection and transmission coefficients are given:

$$r = \frac{s_r}{s_{in}} = \frac{-|a_0|^2 \; j(\omega - \omega_1 - j\frac{1}{\tau_1})}{(\omega - \omega_0 - j\frac{1}{\tau_0})(\omega - \omega_1 - j\frac{1}{\tau_1}) - \kappa_{01}^2}$$
$$t = \frac{s_t}{s_{in}} = 1 + \frac{-|a_0|^2 \; j(\omega - \omega_1 - j\frac{1}{\tau_1})}{(\omega - \omega_0 - j\frac{1}{\tau_0})(\omega - \omega_1 - j\frac{1}{\tau_1}) - \kappa_{01}^2} \quad , \qquad (2.22)$$

As shown in Fig. 2.5 [5], the curves for the three cases with various frequency differences $\delta = \omega_0 - \omega_1$ between the two resonators lead to the different degree of asymmetry, due to the interference between the broadband and narrowband modes.

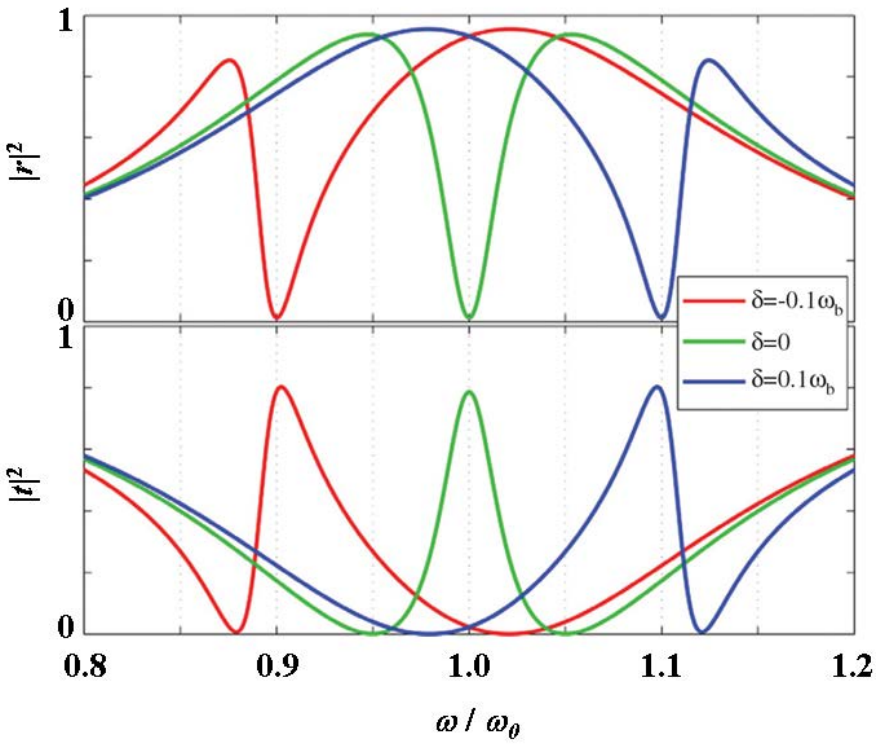

Figure 2.5 Transmission and reflection spectra for various cases of frequency difference between the broadband and narrowband mode, red: δ = -0.1, green: δ = -0, blue: δ = 0.1) [5].

One can also observe that the opposite sign of δ provides asymmetrically shaped spectra of mirror symmetry. For the special case at δ = 0 (green line), there is the emergence of the narrow transparency window, which is due to the Fano interference between the broadband and narrowband modes.

2.5 Summary

In this chapter, various modeling schematics are presented including the perturbation analysis, analogy with coupled oscillators, and coupled mode theory. In the following chapters, I'll introduce the simple and general approach of the coupled mode formalism for the Fano resonances in some specific examples: plasmonic metal-insulator-metal (MIM) waveguide platform with T-junction resonator (details in chapter 3), plasmon-analogue of electromagnetically induced transparency phenomenon with MIM stub-pair structure (details in chapter 4), and the chiral resonator in the circular basis (details in chapter 5).

Chapter 3

Fano Resonance in Plasmonic MIM Waveguide

In this chapter [16], we use coupled mode theory to analyze a metal-insulator-metal (MIM) plasmonic stub structure, to reveal the existence of asymmetry in its transmittance spectra. Including the effect of the near field contribution for the stub structure, the observed asymmetry is interpreted as Fano-type interference between the quasi-continuum T-junction-resonator local-modes and discrete stub eigenmodes. Based on the asymmetry factor derived from the coupled mode theory analysis, methods to control transmittance asymmetry are also demonstrated.

3.1 Introduction

A resonant Fano resonance was originally a quantum mechanical phenomenon [1], which is used to describe asymmetry in ionization spectra of atoms and molecules. The stub structure [33], a short- or open-circuited section attached to a transmission line, plays an important role in microwave engineering, primarily for impedance matching and signal filtering purposes. Due to their compact size and ease of fabrication, stub structures also have received much attention in the nano-photonic area [34-40], including plasmonics applications. For example, utilizing a stub structure in plasmonic MIM waveguide platform, a nanoscale wavelength selective filter [38, 41-43], absorption switches [44, 45], and demultiplexers and waveguide bends of high transmittivity [34, 46] have been demonstrated. Especially, a resonant-less signal filtering function of the stub also has received much attention, alleviating the metallic loss experienced in plasmonic resonator based filters.

With the need for precise analysis of MIM stub structures and related emerging devices, different analytical modeling approaches have been suggested [47-51], including scattering matrix method and microwave transmission-line model. Plasmonics, often treated as the optical analogue of microwave engineering, there also has been good success in extending the

microwave transmission-line theory for a plasmonic stub [34, 47, 50, 51] (as shown in Fig. 3.1). For example, Pannipitiya et. al [47] successfully predicted the characteristics of MIM stub structures with relatively simple formulation, modifying transmission line theory to include metal loss (Fig. 3.1b). Still, for the transmission-line stub-model treating / including the transmission mode only, the effect of real metal through the near field contribution has not been properly explored so far.

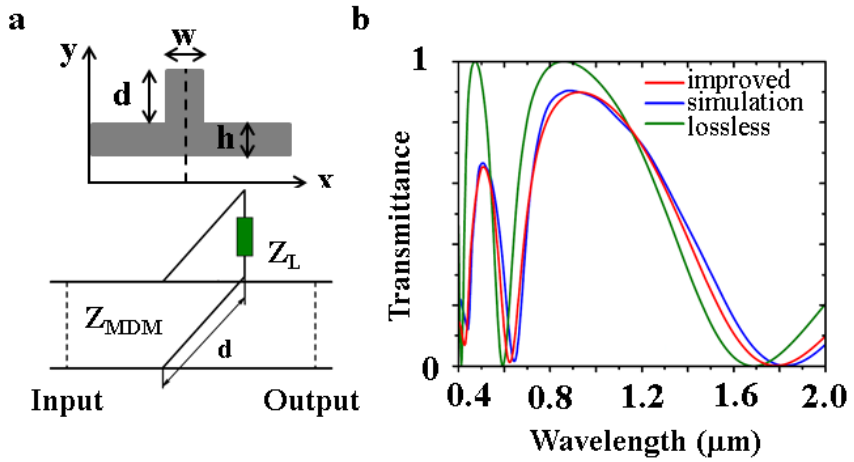

Figure 3.1 (a) Schematics of plasmonic MIM single stub structure (up), and the simplified transmission model including loss (down). (b) Transmittance spectra calculated by the improved transmission model (red), simulation data (blue), lossless model (green) [47].

Here, by assuming a resonator in the cross-section junction of the stub-waveguide structure - to incorporate the contributions from local modes -, we reveal the existence of Fano-type asymmetry [1, 4] in the transmission spectra of the stub, for MIM plasmon waveguides. Solving the CMT for the stub structure by assuming a low-Q resonator in the stub-waveguide T-junction, to account for local modes, we explain the observed asymmetry as the Fano-type mixing between the broadband resonator mode and discrete stub eigenmodes. Deriving the asymmetry factor and key physical parameters from the CMT analysis, we then demonstrate the control of spectral asymmetry in the stub transmittance response. The MIM stub structure, providing controllable Fano-type spectral asymmetry in a convenient waveguide platform, will be useful in the realization of future plasmonic devices, such as low-power, high-contrast optical switches [4, 52-54].

3.2 CMT Analysis of Plasmonic MIM Stub

3.2.1 CMT Modeling of MIM Stub Structure

Fig. 3.2 illustrates the schematics of the simplest MIM single mode ($W << \lambda_{spp}$) plasmonic waveguide stub, used in the study. CMT analysis was carried out, assuming an effective low-Q junction resonator [55, 56] in the cross section

region of the T-junction (in between the plasmonic stub and main waveguide). With the resonator in the T-junction, the stub-waveguide system is now equivalent to T-branch waveguides weakly coupled to the junction resonator. As a result, the transmittance property of the stub becomes affected by the presence of assumed resonator and its resonance characteristics.

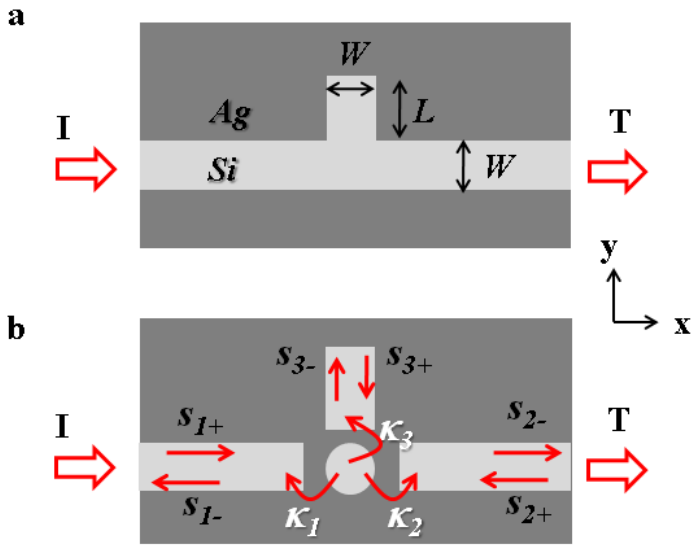

Figure 3.2 (a) Schematics of stub structure. *W* is the width of stub / waveguide, and *L* is stub length. (b) Analytic equivalent model for CMT with an effective low-*Q* resonator in the junction region.

Denoting $\kappa_1 = (2/\tau_1)^{1/2}$, $\kappa_2 = (2/\tau_2)^{1/2}$, and $\kappa_3 = (2/\tau_3)^{1/2}$ as the coupling coefficients between the left / right / stub waveguide branches and the

junction resonator, and also writing $1/\tau_1$, $1/\tau_2$, $1/\tau_3$ as the corresponding decay rates from the resonator to coupling waveguides, the time evolution of field amplitude *a* for the stub-waveguide junction resonator can be written in the following form [27],

$$\frac{da}{dt} = (j\omega_R - \frac{1}{\tau_1} - \frac{1}{\tau_2} - \frac{1}{\tau_3})a + \kappa_1 s_{1+} + \kappa_2 s_{2+} + \kappa_3 s_{3+}) \qquad (3.1)$$

where ω_R is the resonance frequency of the T-junction resonator, and $s_{i\pm}$ being the field amplitudes in each waveguide (i = 1, 2, 3, for outgoing (-) or incoming (+) from the resonator). With the conservation of total power [27], we also dictate

$$s_{i-} = -s_{i+} + \kappa_i a \ . \qquad (3.2)$$

Now, further assuming perfect reflection at the end of the stub of length *L*, we can describe the phase evolution in the stub structure as follows:

$$s_{3+} = s_{3-} \cdot e^{j\phi}, \qquad (3.3)$$

where ϕ = $2\pi \cdot (2L / \lambda)$ is the phase change between the outgoing and incoming wave to the stub (λ represents λ_{spp} for real metal structure, and λ_{air}

/ $n_{\text{dielectric}}$ for PEC structures).

Using Eq. (3.1), (3.2) and (3.3), we then write the transmittance equation for the simplest MIM stub,

$$t = \frac{s_{2-}}{s_{1+}} = \frac{-\kappa_1 \kappa_2}{j(\omega - \omega_R) - \frac{1}{\tau_1} - \frac{1}{\tau_2} - \frac{1}{\tau_3} + \frac{\kappa_3^{\,2}}{1+e^{-j\phi}}} \tag{3.4}$$

where, ω is the operation frequency.

3.2.2 Derivation of Fano Asymmetric Parameter

Now, for a sufficiently narrow ($W << \lambda_{spp}$) and long ($L > \lambda_{spp}$) stub, in good approximation we set $\tau_1 \sim \tau_2 \sim \tau_3$ as τ_0, and use $\kappa_0 = (2 / \tau_0)^{1/2}$ to get,

$$t = \frac{2}{j(\omega - \omega_R)\tau_0 + 3 - \frac{2}{1+e^{j\phi}}} \tag{3.5}$$

For Eq. (3.5), here we define the asymmetry factor A_R, as;

$$A_R \equiv (\omega - \omega_R)\tau_0 = 2(\omega - \omega_R) / \Gamma_0 \tag{3.6}$$

where Γ_0 is the full width at half maximum bandwidth for the resonator-to-stub coupling.

Using A_R, we then rewrite the transmittance coefficient T for the stub structure, to arrive to the result of our CMT analysis;

$$T = |t|^2 = \frac{4(\cos\phi + 1)}{(A_R{}^2 + 3)(\cos\phi + 1) + 2 + 2A_R \sin\phi} \tag{3.7}$$

As can be seen in Eq. (3.7), depending on the sign of the phase term $sin\phi$ = $sin(2L \cdot (2\pi / \lambda))$ *around the stub operation frequency*, the stub transmittance becomes to have spectral asymmetry - for its asymmetry strength determined by A_R.

It is worth noting that A_R can be approximated as a constant for a given structure around the operation frequency of interest $\omega \sim \omega_T$, since Γ_0 of the low-Q junction resonator is much larger than the bandwidth of the stub, and then $A_R = 2(\omega - \omega_R) / \Gamma_0 \sim 2(\omega_T - \omega_R) / \Gamma_0 + o(\delta\omega / \Gamma_0)$.

Most importantly, noting that A_R measures the Γ_0 - normalized distance between the operation frequency $\omega \sim \omega_T$ and the resonant frequency ω_R of the broadband junction resonator, the asymmetry factor increases if the phase deviation between two frequencies involved in the Fano process increases.

3.3 Interpretation of Fano-type Spectral Asymmetry in MIM stub

Figure 3.3 shows the FDTD obtained transmittance spectra from the stub, overlaid to the analytical CMT solution (Eq. (3.7)) with the fitting parameter A_R. MIM waveguides, composed of *Ag* or PEC sandwiching Si layer (W = 30nm) have been assumed in the analysis. To incorporate the dispersion of Ag permittivity, Drude model, which is reasonably accurate within 1 ~ 2 μm wavelength range, is applied.

For the operation frequency near ω_T = 193.5THz (λ_{air} = 1550nm), two stub structures with different stub length L (440nm, 810nm) returned perfect fit with an *identical asymmetry factor* of A_R = - 0.8 for those assumed *identical T-junction resonators* justifying the use of resonator local modes (determined by the T-junction structure) in the analysis. Compared to the symmetric (A_R = 0) spectra from the PEC-Si-PEC waveguide stub (note that τ_0 and $\Gamma_0 = \infty$ for PEC, as local surface plasmon modes are absent and only propagation modes exist, leading to $A_R = 2(\omega - \omega_R) / \Gamma_0 = 0$), the asymmetric spectral profile of the Ag-Si-Ag stub is evident, derived from the Fano-type mixing of quasi-continuum resonator local modes and discrete eigenmodes of the stub.

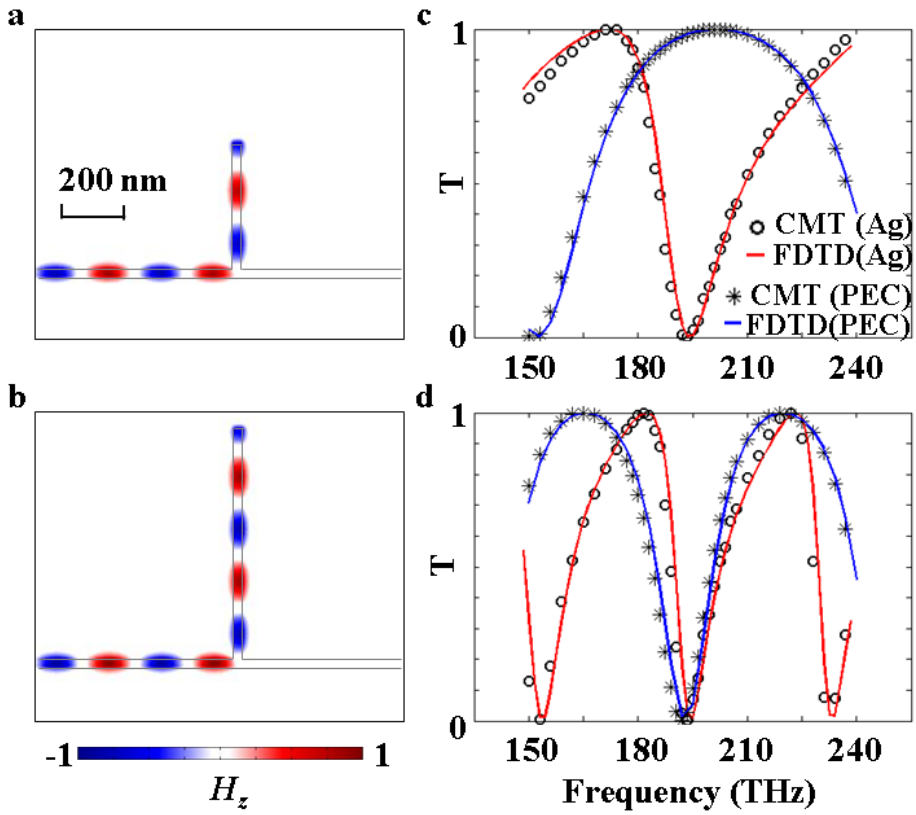

Figure 3.3 Field patterns of plasmonic MIM (*Ag-Si-Ag*) stub structures, at the operation frequency ω_T = 193THz. Waveguide width *W* was set to 30 nm. Stub length $L = (5/4\lambda_{spp}$ and $9/4\lambda_{spp}) - \delta_{skin\text{-}depth}$ for FDTD was set at, (*a*) 440 nm and (*b*) 810 nm. Corresponding transmittance spectra are shown in (*c*) and (*d*), calculated either with CMT (marks) or FDTD numerical analysis (lines). $A_R = 0$ for PEC and $A_R = -0.8$ for real metal.

3.4 Control of Fano Resonance in MIM stub

Also interesting to investigate is the functional form of the asymmetry factor A_R, from which we can devise a means to enhance the asymmetry of the resonance, for example, by adjusting $\omega \sim \omega_T$, ω_R, or Γ_0.

3.4.1 Dependency on the Refractive Index of the Junction

Directly modifying the T-junction resonator (ω_R or ω_0), the asymmetry of the transmittance can be controlled. Figure 3.4d – 3.4f show the transmittance spectra obtained from the *same* plasmonic stub-waveguide *structure* (L = 440 nm, W = 30 nm, $\omega \sim \omega_T \sim$ 193 THz), *yet with different refractive index* (n = 1, 3.46, and 5 for Fig 3.4a, 3.4b, and 3.4c) in the junction resonator region. The asymmetry factor A_R was found to be 0, -0.8, and -1.7, for the junction resonator index of n = 1, 3.46, and 5, respectively. Stronger asymmetry in the transmittance spectra, accompanied by the pronounced emergence of local modes (insets in Fig. 3.4, calculated with COMSOL Multiphysics 3.5) is evident for the index-raised-resonator stub structures.

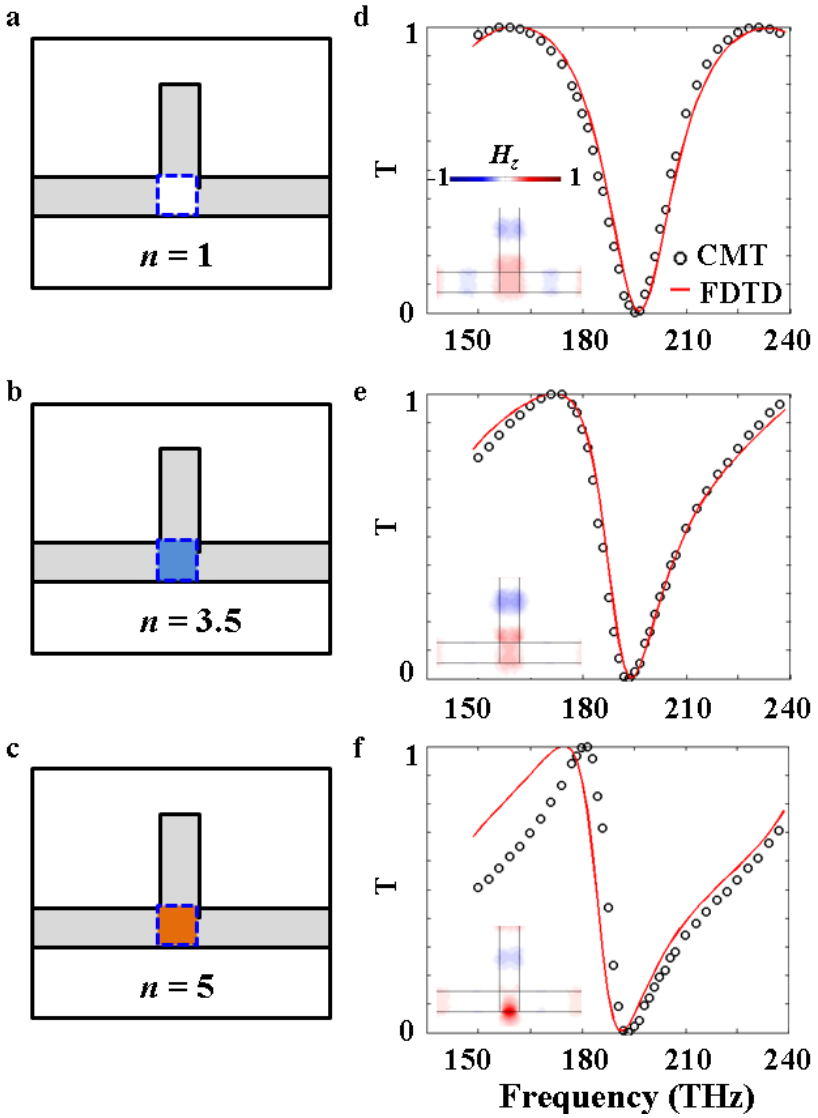

Figure 3.4 Stub structures with different refractive index n in the junction resonator region; (*a*) n = 1, (*b*) n = 3.46, and (*c*) n = 5. Transmittance spectra from stub (*a*)~(*c*) are shown in (*d*)~(*f*). Insets show the zoomed-in local mode profiles around the junction resonator. The values of A_R used in the CMT was 0 (for n = 1), - 0.8 (for n = 3.46), and - 1.7 (for n = 5), respectively.

3.4.2 Dependency on the Stub Length

Instead of modifying the resonator structure as above, the ω_T dependence of A_R can be used to control the asymmetry. By tuning the stub length L, it is possible to adjust the stub operation frequency ω_T. Figure 3.5 shows the structure and transmittance spectra of the stubs, for ω_T = 150 THz (L = 580 nm), 200 THz (L = 440 nm), and 300 THz (L = 260 nm), respectively. Increased asymmetry was observed from A_R = - 0.5 to - 0.8 and - 1.2, with the increase of ω_T.

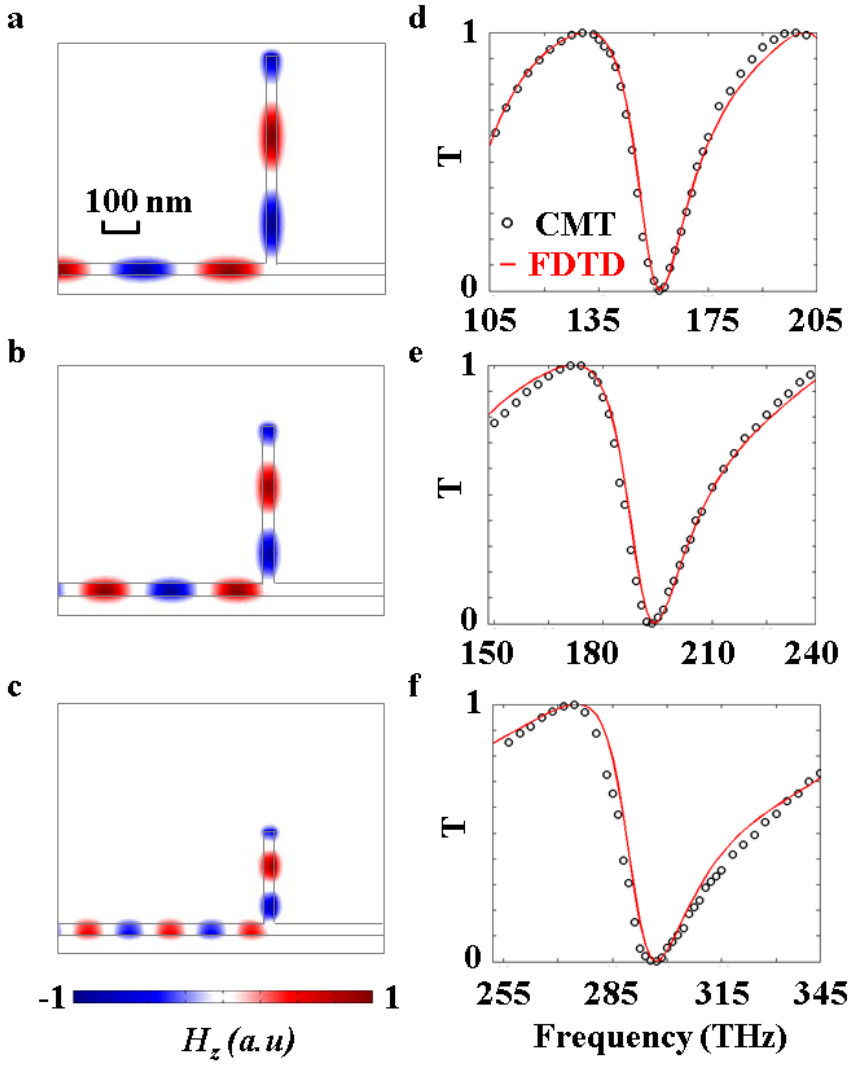

Figure 3.5 Stub structures (*Ag-Si-Ag*) and field profiles at different operation frequencies; (*a*) ω_T = 150 THz, (*L* = 580 nm), (*b*) ω_T = 193 THz (*L* = 440 nm), and (*c*) ω_T = 300 THz (*L* = 260 nm). Transmittance spectra from the stub structures of (*a*) ~ (*c*) are shown in (*d*) ~ (*f*). The values of asymmetry factor A_R used in the CMT calculation were -0.5, -0.8, and -1.2, respectively.

3.5 Summary

By including the local field contribution for the exact analysis of real-metal plasmonic MIM stub, we develop a temporal coupled mode theory to reveal the existence of Fano-type asymmetry in the stub transmittance spectra. Perfect fit with the results of FDTD numerical analysis was observed for various stub geometries and operation conditions, validating the theoretical analysis. We also derive the asymmetry factor A_R for the MIM stub from the analytical CMT model, which could be used to control the degree of asymmetry by various means. Tuning of the asymmetry factor A_R, from 0 to -1.7 was achieved by employing different refractive index materials in the junction resonator, or by changing the stub operation wavelength. Our analytical model for the exact analysis of the MIM plasmonic stub, and findings for the existence of, controllable asymmetry in their transmittance spectra will stimulate the design of low power optical switching devices, in convenient plasmonic waveguide platforms.

Chapter 4

Plasmon-Induced Transparency in MIM Stub Pair

In this chapter [17], we derive a governing equation for spectral asymmetry in electromagnetically induced transparency (EIT). From the key parameters of asymmetry factor –namely dark mode quality factor Q_d, and frequency separation between bright and dark mode $\omega_{bd} = \omega_b - \omega_d$–, a logical pathway for the maximization of EIT asymmetry is identified.

By taking the plasmonic metal-insulator-metal waveguide as an implementation platform, a plasmon-induced transparency (PIT) structure of tunable frequency separation ω_{bd} and dark mode quality factor Q_d is suggested

and analyzed. Compared to previous works on MIM-based plasmon modulators, an order of increase in the performance figure (12dB contrast with ~60% throughput) is achieved from the highly asymmetric, narrowband PIT spectra.

4.1 Introduction

Usually manifesting itself in a three-level system, the highly narrow pass-band spectrum of electromagnetically induced transparency is the result of destructive interference between a bright (broadband) absorption band and a dark (narrowband) resonance state [57]. Supporting a strongly dispersive and narrow pass-band in an opaque medium [58], EIT has been widely studied and used in slow light [59-61], or sensor applications [62, 63]. EIT has also been implemented in other platforms, such as electric circuits [64], coupled micro-resonators [65, 66], plasmonic [67-69], and metamaterial structures [70, 71]. In general, due to the interference between the excitation pathways for bright mode and dark mode, the resultant EIT spectrum is naturally Fano-asymmetric, unless two modes are degenerate, as observed in quantum systems [1, 58, 71], coupled resonators [64], plasmonic systems [4, 16, 44, 65, 72-77], and metamaterials [61, 67, 70]. Meanwhile, it is well-understood that this spectral asymmetry would compose one of the

critical factors in the application of EIT (such as low-power, high-contrast optical switches or sensors), together with the transmittance and bandwidth of the dark mode; nonetheless, most of the prior works have focused only on the realization of EIT in different platforms, setting aside the issue of asymmetry in phenomenological description level.

In this chapter, we focus on the control of Fano asymmetry in EIT. By analytically deriving an EIT-asymmetry factor, key routes for the maximization of EIT-asymmetry are identified: use of dark mode having maximum quality factor Q_d, and maximization of the frequency separation $\omega_{bd} = \omega_b - \omega_d$ between the bright and dark mode. We then suggest one platform of EIT, a stub-pair in the MIM waveguide, supporting a tunable ω_d and a fixed ω_b mode of mutual orthogonality for the maximization of ω_{bd}. To activate the coupling from bright to the dark mode through quasi-orthogonal mode overlap, symmetry offset in the stub-pair structure is exploited. As a result, highly asymmetric and narrowband PIT spectra are realized, even with the inclusion of metal loss. A feasibility study of the structure as a plasmonic MIM waveguide modulator shows unprecedented performance figures (throughput and modulation depth) at an order higher than previous works [44, 77], proving the importance of asymmetry control in EIT applications.

4.2 Fano Asymmetry in EIT

4.2.1 Theoretical Background of EIT

The first experimental demonstration of EIT was provided in 1991 by Boller et al. [57], with the transmittance of an ultraviolet transition to an autoionizing state of Sr vapor (Fig. 4.1).

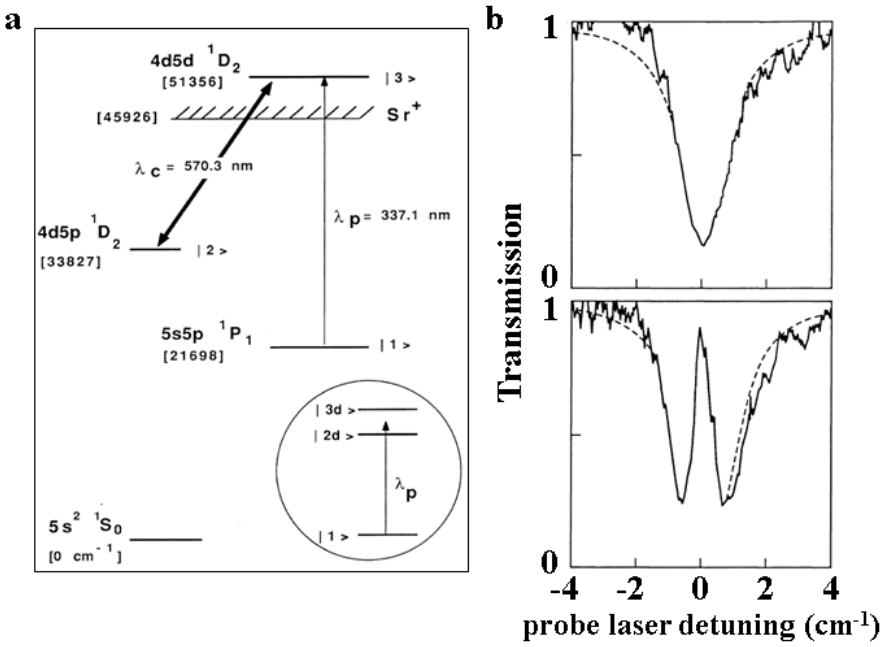

Figure 4.1 (a) Energy-level diagram of neutral Sr. Inset shows dressed state picture. (b) Transmission profile with a completely opaque atomic cell without the coupling field λ_c (top), and a narrow transparency window with the coupling field λ_c (bottom) [57].

The top figure shows the absorption profile with a completely opaque atomic cell. However, by applying a coupling field (λ_c) opens up a narrow transparency window because of the amplitude interference between the two transition paths. Due to the strongly dispersive pass-band, this phenomena has received much attention and the analogy of EIT has been demonstrated on various platforms, such as coupled micro ring resonators [64, 66], plasmonic metamaterials [61, 63, 67, 70].

4.2.2 Naturally Asymmetric Spectral Response of EIT

Figure 4.2a illustrates the schematic of a generic EIT system, represented with bright-state ($|\psi_b\rangle$) and dark-state ($|\psi_d\rangle$) resonators. Using the coupled mode theory (CMT) and denoting κ_{ib} and κ_{bd} as coupling coefficients between the incident-bright mode and the bright-dark mode respectively, the derivation for the transmittance of the system is straightforward [27, 29]. When neglecting the system loss, the transmittance T is expressed as,

$$T = 1 - \frac{1}{1 + [\omega - \omega_b - |\kappa_{bd}|^2 / (\omega - \omega_d)]^2 / \kappa_{ib}} \quad . \qquad (4.1)$$

It is worth mentioning that Eq. (4.1) is naturally asymmetric in its frequency response, as T is an odd function of ($\omega - \omega_d$) except for the special case of

degeneracy ($\omega_b = \omega_d$). In order to derive an analytical expression for the degree of EIT asymmetry, we examine the generic spectra of the transmittance (Fig. 4.2b) and then define the degree of spectral asymmetry F to be $\Delta\omega_{high} / \Delta\omega_{low}$, the ratio of high / low frequency transmission bandwidths (peak-to-node).

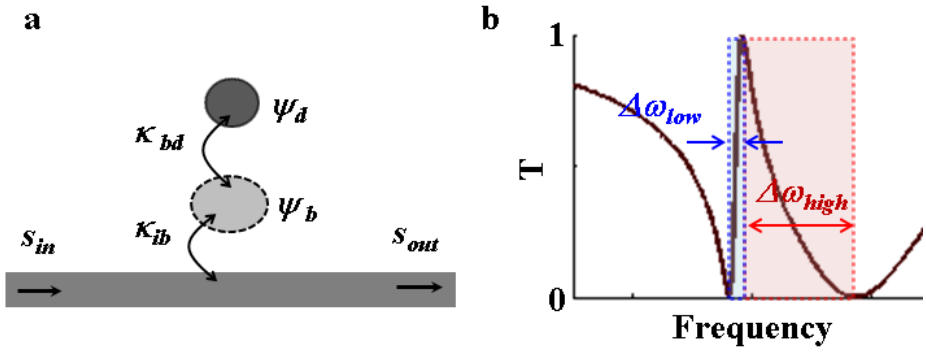

Figure 4.2 (a) Schematics of a generic EIT system, represented as coupled dark- and bright-mode resonators. (b) Definition of F (degree of spectral asymmetry) for EIT.

By taking the differential $dT / d\omega$ to determine the positions of the transmission peak and nodes, the derivation of F is straightforward. Especially if we introduce a Fano-like asymmetry factor by setting $\rho = (\omega_b - \omega_d) / (2\kappa_{bd})$, F becomes a function of ρ only:

$$F(\rho) = \frac{\sqrt{\rho^2 + 1} + \rho}{\sqrt{\rho^2 + 1} - \rho}. \qquad (4.2)$$

It is critical to mention that since $F(\rho)$ is a monotonic function of ρ (as $dF(\rho)$ / $d\rho > 0$, Fig. 4.3), an increase of $\rho = \Delta\omega_{bd} / (2\kappa_{bd})$ would equivalently lead to the increase of the EIT asymmetry. Specifically, a maximum asymmetry would be obtained using a dark mode with negligible couplings to incident- or bright-mode ($\kappa_{id} \sim \kappa_{bd} \sim 0$), and by employing at the same time a bright mode having widest bandwidth, as $\max(\Delta\omega_{bd}) \sim \Delta\omega_b / 2$, for ω_d approaching $\omega_b \pm \Delta\omega_b / 2$. For example, a frequency-tunable dark mode (ω_d) of near-zero coupling κ_{bd} to the frequency-fixed widest-bandwidth bright mode (ω_b) could be used for the control or maximization of F. Finally, we note that our definition of the EIT asymmetry factor ρ is in line with the interpretation of the Fano q parameter [1, 4, 16], yet the latter further holds for non-zero coupling κ_{id} between the incident field and discrete mode, unlike the present case of EIT ($\kappa_{id} \sim 0$).

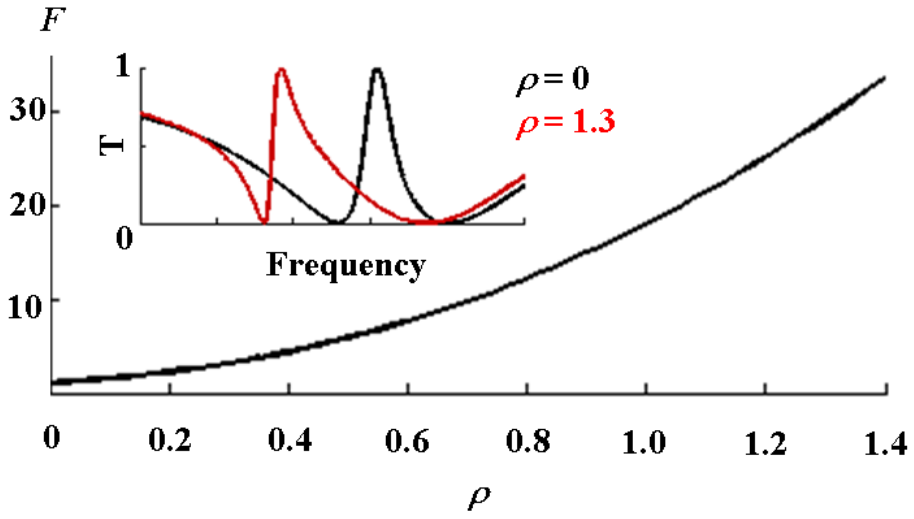

Figure 4.3 Behavior of F as a function of the asymmetry factor $\rho = (\Delta\omega_{bd}/(2\kappa_{bd})$. Inset shows EIT transmittance at different values of ρ = 0 and 1.3 respectively.

4.3 Realization and Control of Fano Asymmetry in Plasmon-Induced Transparency

4.3.1 Plasmon-Induced Transparency

For the implementation of the idea, we employ a plasmonic platform based on a MIM (*Ag-SiO$_2$-Ag*) waveguide. Figure 4.4a shows a MIM stub pair coupled to a waveguide of width w_w composing our suggested PIT structure, which provides a bright- and a dark-mode based on the *symmetric*- (Fig. 4.4b) and *anti-symmetric*- (Fig. 4.4c) stub modes, under the *y*-axis *symmetric* waveguide *incident*-mode excitation. In order to open a channel of small κ_{bd}

between the *bright* (symmetric) and *dark* (anti-symmetric) mode, a perturbation of $\Delta L << L_0$ to the symmetric stub-pair is imposed to make the frequency-split bright modes of $\omega_{b\pm} \sim 1/L_{1\pm}$ ($L_{1\pm} = L_0 \pm \Delta L$) to be quasi-orthogonal ($\kappa_{bd} \neq 0$) to the dark mode of $\omega_d \sim 1 / (2L_0 + w_w)$.

Here, it is critical mentioning that the resonant frequency of bright-mode ω_b depends on L_0 and ΔL, while the frequency of dark-mode ω_d is a function of L_0 and waveguide width w_w. Therefore, for a given value of ΔL, by adjusting w_w, it becomes possible to shift ω_d (at fixed ω_b) to achieve the maximization of $\Delta\omega_{bd}$ (and $F(\rho)$). In addition, we also note that the largest κ_{ib} and thus maximum $\Delta\omega_b$ is attained by proactively matching the impedance between the stub and waveguide, with the use of the same waveguide width w_w and stub width w_s ($w_w = w_s = w$).

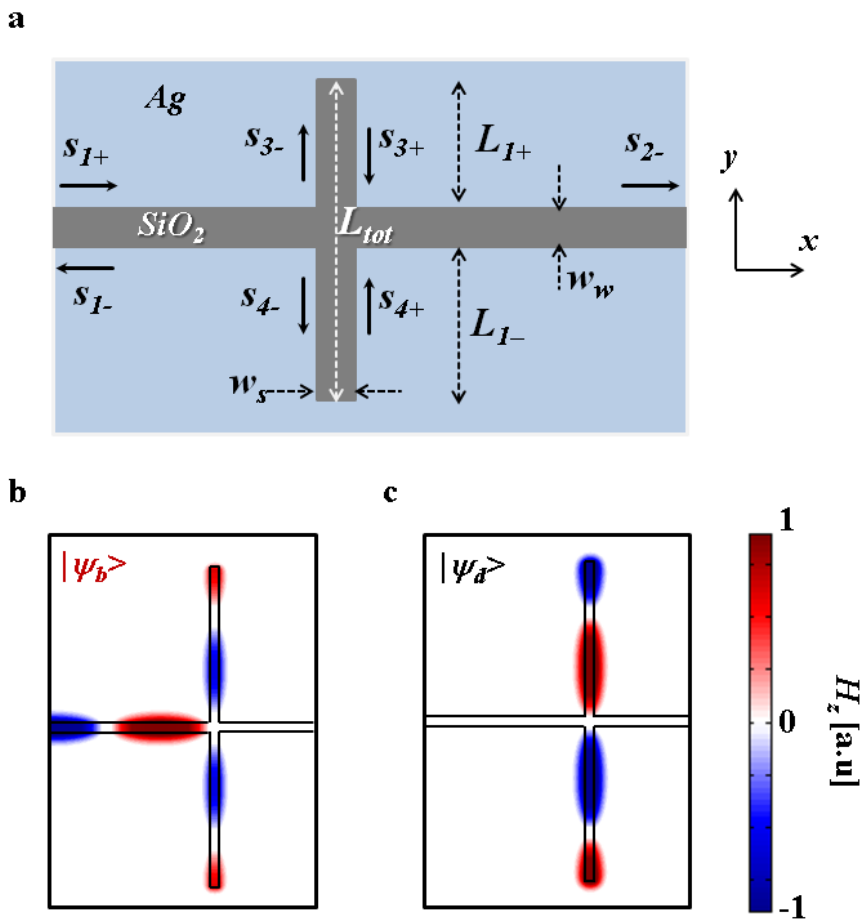

Figure 4.4 (a) Schematics of an MIM stub-pair PIT system. Field (H_z) distributions for the (b) symmetric bright mode ($|\psi_b>$), and (c) anti-symmetric dark mode ($|\psi_d>$).

Figure 4.5 compares the behavior of $\omega_{b\pm} \sim 1 / (L_0 \pm \Delta L)$, (red lines, ΔL = 20 nm); and $\omega_d \sim 1 / (2L_0 + w)$ (black line from analytic, red circle from COMSOL, *Ag* parameters using [78]) under the control of w (from w = 30 nm

to 300 nm). With the increase of w, a larger frequency separation $\Delta\omega_{bd}$ is evident. As can be seen from the insets in Fig. 4.5, the strong E_x intensity distribution in the junction region for $|\psi_d\rangle$ again visually explains the dependency in w for the dark mode, in contrast to that of $|\psi_{b\pm}\rangle$.

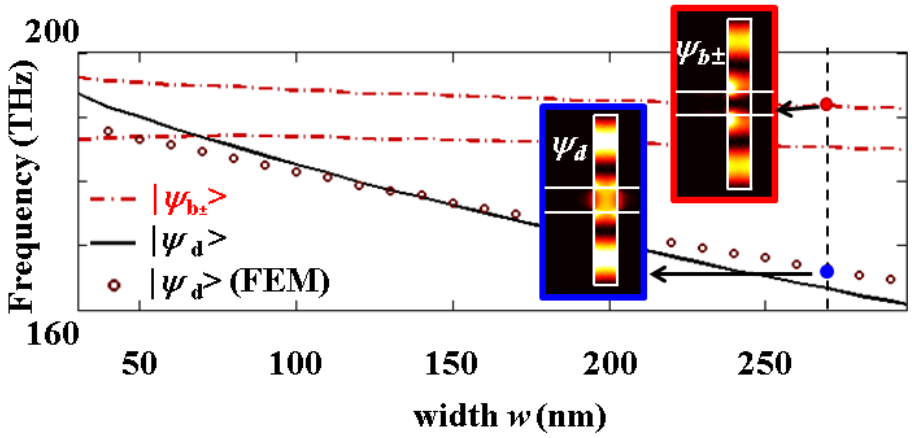

Figure 4.5 Resonant frequencies of $|\psi_{b\pm}\rangle$ and $|\psi_d\rangle$ are plotted as a function of stub width w (varies from 30 to 300 nm); $\omega_{b\pm} = m{\cdot}c\,/\,(n_{eff}\ \cdot L_{1\pm})$ (in red dotted lines), and $\omega_d = 2m \cdot c\,/\,(n_{eff} \cdot L_{tot})$ (black line). The difference of stub length ΔL is fixed at 20 nm, and $L_0 = m \cdot \lambda_{spp}$ (modal number m = 3/4) are applied with the effective surface plasmon polariton wavelength λ_{spp}, calculated from λ_0 / n_{eff}, at λ_0 = 1550 nm. The two Insets show the x-polarized electric field intensity ($|Ex|^2$) distributions for $|\psi_{b\pm}\rangle$ and $|\psi_d\rangle$ mode respectively.

4.3.2 CMT modeling of Asymmetric PIT in MIM Stub Pair

Upon identifying key parameters for the maximization of spectral asymmetry and also establishing a PIT platform for its implementation, we now work on the verification of the suggested idea by using both analytic CMT and numerical analysis. For the CMT analysis, we treat the stub-junction region as an ultra-low-*Q* resonator [16], and write down an equation to represent the interaction between the stub-junction resonator and adjacent waveguides,

$$\frac{da_0}{dt} = (j\omega_0 - \sum_p \frac{1}{\tau_p})a_0 + \sum_p \kappa_p s_{p+} \ , \tag{4.3}$$

together with equations for energy conservation [16, 27]

$$s_{p-} = -s_{p+} + \kappa_p^* a_0 \ , \tag{4.4}$$

where $s_{p\pm}$ is the field amplitude in waveguide p = 1 ~ 4, coupling into (+) or out of (-) the resonator (of field amplitude a_0 and resonant frequency ω_0), and κ_p (= $(2 / \tau_p)^{1/2}$ [16, 27]) is the coupling coefficient between the junction resonator and adjacent waveguides.

By noting that the dark-mode $|\psi_d\rangle$ extending over waveguides 3 *and* 4 couples to bright modes $|\psi_{b+}\rangle$ and $|\psi_{b-}\rangle$ solely occupying waveguides 3 and 4

respectively, we write:

$$\frac{da_d}{dt} = (j\omega_d - \frac{1}{\tau_{d3}} - \frac{1}{\tau_{d4}})a_d + \kappa_{bd3}s_{3-} + \kappa_{bd4}s_{4-}, \tag{4.5}$$

$$s_{3,4+} = (s_{3,4-} - \kappa^*_{bd3,4}\, a_d) \cdot e^{-j\phi_{3,4}}, \tag{4.6}$$

where $\phi_p = 2\pi \cdot (2L_p / \lambda_{spp})$, $\lambda_{spp} = \lambda_0 / n_{eff}$; and $\kappa_{bd3(4)}$ is the coupling coefficient between the dark mode resonator (of field amplitude a_d and resonant frequency ω_d) and the field $s_{3(4)-}$, coupling from the junction region into the dark mode resonator residing in the stub region.

Solving Eq. (4.3) ~ (4.6) for s_{3+} and s_{4+}, and then applying boundary conditions of $s_{1+} = 1$ and $s_{2+} = 0$ with first-order approximations of $\tau_1 \sim \tau_2 \sim \tau_3 \sim \tau_4 \sim \tau_0 \sim 0$ (for ultra-low Q junction resonator) and $\tau_{d3} \sim \tau_{d4} \sim \tau_d$ ($\Delta L << L_0$). Then for $p = 3$ (or 4), and $q = 4$ (or 3) we get:

$$s_{p(q)+} = \frac{(j(\omega-\omega_0) - 2/\tau_d)(e^{j\phi_q} + 1)}{(j(\omega-\omega_0) + 2/\tau_d) \cdot (e^{j\phi_p} + e^{j\phi_q} + 2e^{j(\phi_p+\phi_q)})}. \tag{4.7}$$

Now using $t = s_{2-}/s_{1+} = s_2$ ($s_{1+} = 1$) and since $s_{2-} = \kappa^* a_0$, by expressing a_0 in terms of s_{3+} and s_{4+} using Ea. (4.3) we finally arrive at the PIT transmittance T of the system:

$$t = \frac{\kappa^* \cdot \sum_p \kappa_p s_{p+}}{j(\omega - \omega_0) + \sum_p 1/\tau_p} \cong \frac{2/\tau_0 (s_{1+} + s_{2+} + s_{3+} + s_{4+})}{j(\omega - \omega_0) + 4/\tau_0}, \qquad (4.8)$$

$$T = |t|^2 = \left| \frac{jA_d (e^{j\phi_3} + e^{j\phi_4} + e^{j(\phi_3+\phi_4)} + 1) + e^{j(\phi_3+\phi_4)} - 1}{(jA_d + 1)(e^{j\phi_3} + e^{j\phi_4} + 2e^{j(\phi_3+\phi_4)})} \right|^2 . \qquad (4.9)$$

where $A_d = (\omega - \omega_d) \cdot \tau_d / 2$ represents the Fano asymmetry parameter.

4.3.3 Control of Spectral Asymmetry of PIT

The black lines in Fig. 4.6d – 4.6f show the plot of the transmittance *T* using the CMT result of Eq. (4.9). It is worth noting that the metallic loss of *Ag* has been incorporated in the equation through the phase evolution terms $\phi_p = 2\pi n_{eff} \cdot (2L_p / \lambda_0)$, with n_{eff} extracted from the MIM waveguide analysis using COMSOL Multiphysics.

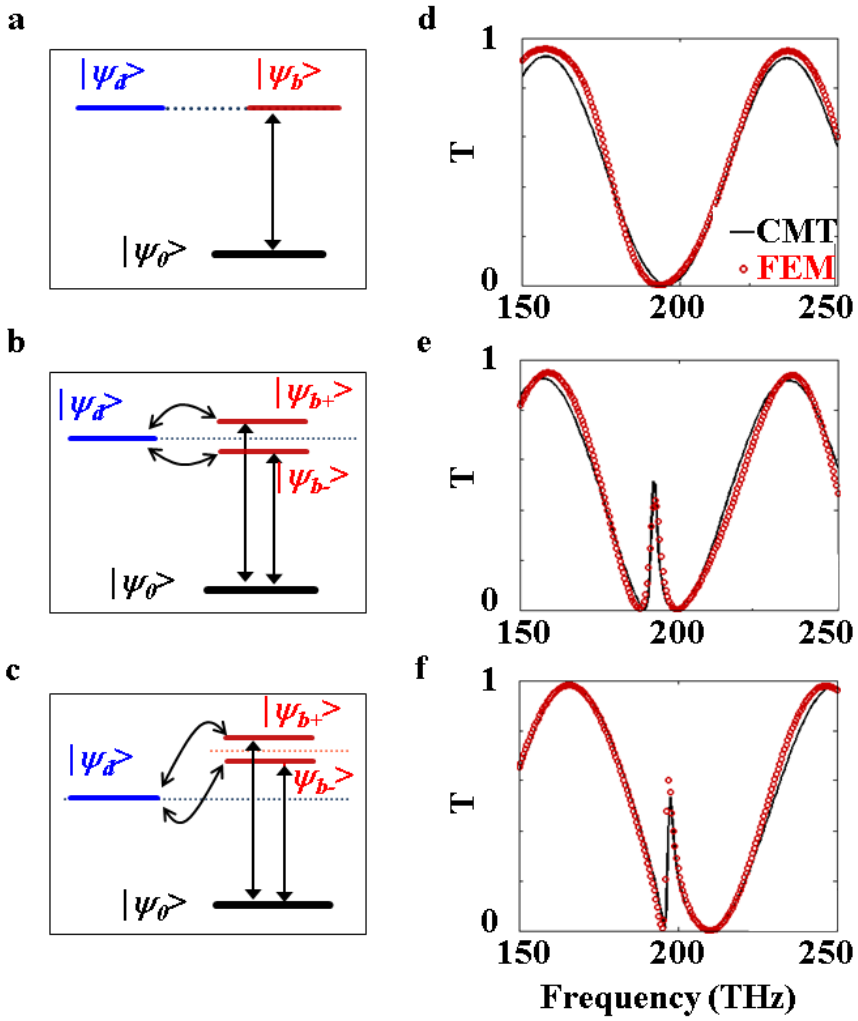

Figure 4.6 Schematics of energy levels of bright state $|\psi_{b\pm}\rangle$ and dark state $|\psi_d\rangle$ and transmittance (T) spectra from CMT (lines) and COMSOL (markers) for each structure (a, d), for ΔL = 0 and w = 40 nm; (b, e) ΔL = 20 nm and w = 40 nm; (c, f) ΔL = 20 nm and w = 80 nm. Here $L_{\pm} = 5/4\ \lambda_{spp} \pm \Delta L$..

A perfect fit in the PIT spectra between the CMT and numerical calculation results have been achieved, by using two fitting parameters of ω_d and ω_d obtained from the numerical result. As expected, without a perturbation to the structural symmetry (i.e., case of ΔL = 0, Fig.4.6a and Fig. 4.6d), the dark mode excitation is inhibited (as κ_{bd} = 0). In contrast, with a perturbation of ΔL = 20 nm (Fig. 4.6b and Fig. 4.6c) to the symmetric stub-pair, the excitation of the dark mode is evident.

Finally, with the increase of the MIM waveguide width w (40 nm and 80 nm for Fig. 4.6e and Fig. 4.6f respectively), dramatic changes in the PIT-asymmetry $\rho \sim \omega_b - \omega_d(w)$ were observed, as expected. It is worth mentioning that by employing a higher refractive index material in the waveguide-stub junction region to increase the *effective* junction width w_{eff}, it was possible to obtain equivalent results.

4.4 MIM Plasmonic Modulator

4.4.1 Schematics of the MIM Modulator

Utilizing the steeper side of asymmetric PIT spectra, we now study the performance of our structure as an MIM waveguide plasmonic modulator (Fig. 4.7a), by using a voltage-controlled electro-optic polymer in the waveguide for the shift of the PIT transmission peak (dashed line in Fig. 4.7b, for 2 V

bias. Δn = 0.008 [77]).

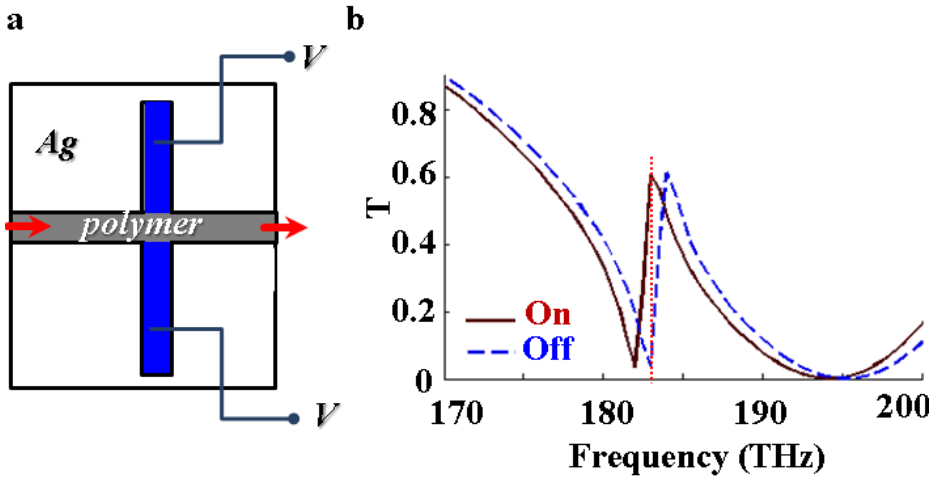

Figure 4.7 (a) Schematic diagram of Plasmonic MIM modulator; the refractive index of electro-optic polymer in the stub region can be controlled with the overlaid electrodes [77]. (b) Transmittance spectra from the modulator in on (black, V_{op} = 0 V) and off (blue, V_{op} = 2 V) states.

Under the application of bias, the switching action of the modulator is evident from Fig. 4.8a (on-state) and Fig. 4.8b (off-state).

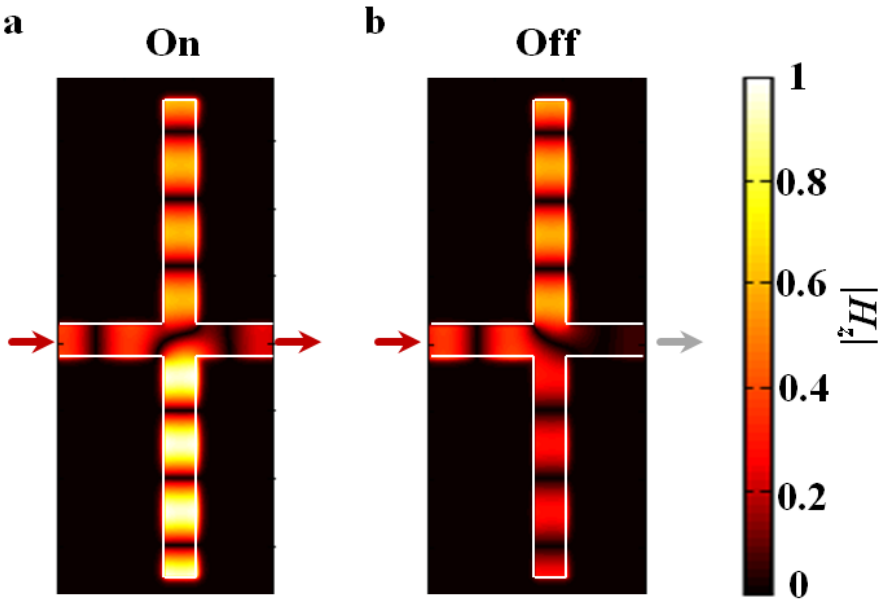

Figure 4.8 Magnetic field amplitude ($|H_z|$) distribution of the modulator in (a) on state, and (b) off states (w = 230 nm, ΔL = 25 nm, ΔV = 2 V).

4.4.2 Optimization of the Structure

Defining the figure of merit (FOM) of the modulator as T / M (T = throughput, M = modulation depth = T_{off} / T_{on}), the parameter scanning for an optimal stub-waveguide structure has been carried out. Figure 4.9 and 4.10 show 'FOM' 'and Throughput' of the modulator plotted as a function of w and ΔL. An impressive FOM value of 9.5 was achieved with excellent throughput (M = – 12.3 dB, T = 60 %) with the parameter set of w = 230 nm and ΔL = 25 nm; which is an order higher than the previous record of FOM = 1 (M = – 3 dB, T

= 50 %) [24].

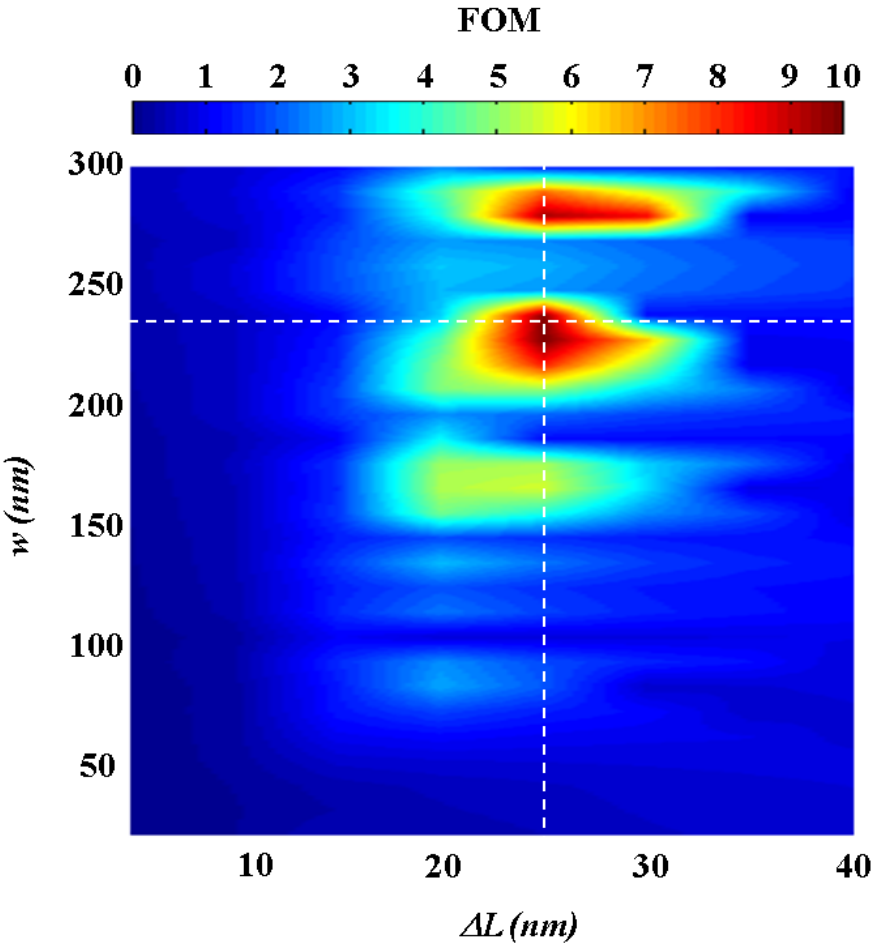

Figure 4.9 FOM of the MIM modulator as a function of *w* (30 nm ~ 300 nm) and *ΔL* (5 nm ~ 40 nm). Crossing dashed lines show the optimized geometric parameters with maximum FOM value (9.5) of *w* = 230 nm, and *ΔL* = 25 nm.

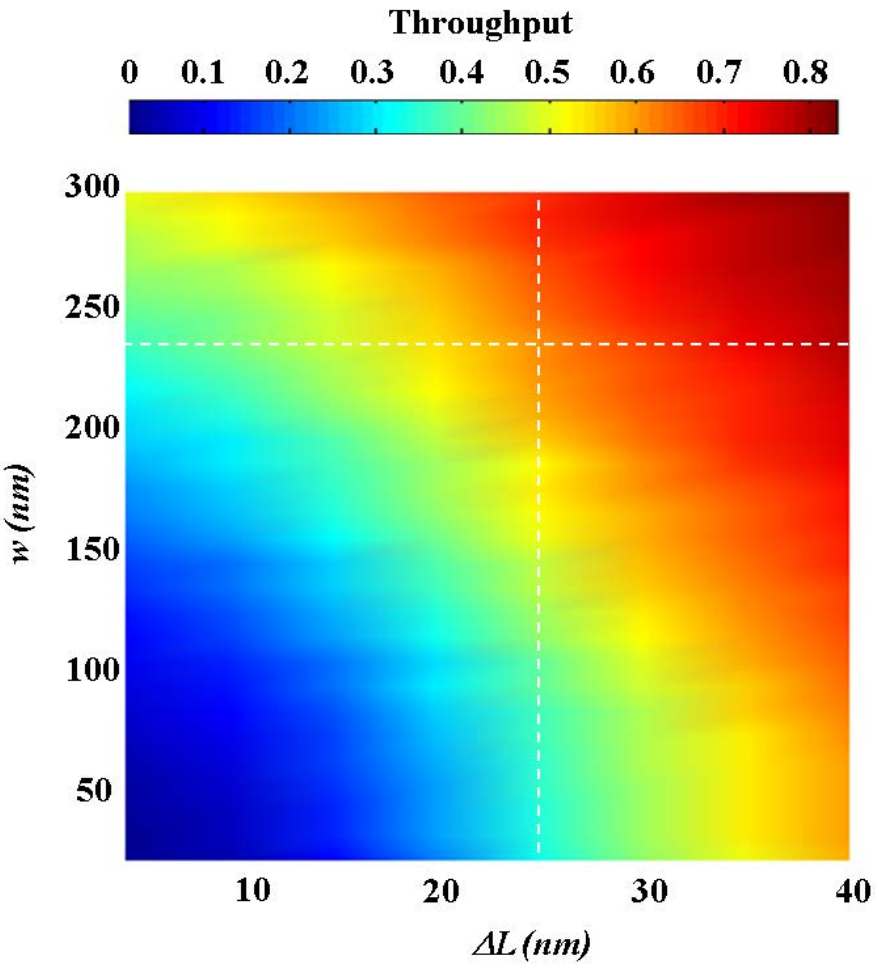

Figure 4.10 Throughput of the MIM modulator as a function of w (30 nm ~ 300 nm) and ΔL (5 nm ~ 40 nm). Crossing dashed lines show the throughput (~ 60 %) at the maximum FOM value (= 9.5) of w = 230 nm, and ΔL = 25 nm.

4.5 Summary

In this chapter, we demonstrated the control and maximization of spectral asymmetry in EIT, through the tuning of key parameters obtained from the analytically derived asymmetry factor. For the real implementation, we proposed an MIM-waveguide-coupled symmetric stub pair, with a perturbation of its spatial symmetry. Application to a plasmonic waveguide modulator showed an order of improvement in its figure of merit when compared to previous records, proving the importance of asymmetry control in the EIT spectrum. We note that our general CMT derivation of EIT asymmetry factor ρ and consequent findings should be applicable to other platforms of EIT or EITs of multiple dark modes – not limited to plasmonics – for the purpose of designing devices which require extremely narrowband and asymmetric spectra, such as low-power high-contrast switches, high-sensitivity sensors, or slow-light based optical buffers.

Chapter 5

Fano Resonance Induced Optical Spin Excitation

In this chapter, a novel route to optical spin excitation based on the mixing of spin-dependent antisymmetric Fano resonances will be introduced. By developing a spin-form coupled mode theory, the origin of the spin-dependent Fano response is clarified in terms of the spin-dependent temporal phase shift, which is the result of counter-rotating spin eigenvectors. An analytical expression of a complex Fano parameter is derived to enable quantitative analysis of the Fano-induced spin excitation. As an application, we demonstrate optical spin switching utilizing the extreme spectral sensitivity of

the spin-density reversal. These results pave a path toward the conservative spectral separation of spins without the need for the magneto-optical effect or chiral loss.

5.1 Introduction

A resonant Fano resonance was originally a quantum mechanical phenomenon, which is used to describe asymmetry in ionization spectra of atoms and molecules. This study is the first to propose *conservative and nonmagnetic* excitation of optical *spin angular momentum* (SAM) [79], based on *spin-dependent* Fano resonances. The control of optical SAM has been a topic of significant attention, not only to access the handedness of biological or chemical media with 'chiral' light-matter interactions but also to open a new domain of optics: such as topological photonics based on the handedness in photonic bandgaps. Because light with different SAMs can be distinguished in materials with electric and magnetic mixing, a.k.a. chiral materials, continuous effort has been made to impose optical SAM by achieving large optical chirality in artificial materials, e.g., nature-mimetic 3-dimensional chirality with metallic helices [80-85] or twisted stacking [82, 85], planar chirality with circular dichroism [86, 87], or gyrotropic materials [84, 88].

However, despite its intrinsic SAM modes, a chiral material alone cannot establish sufficient conditions for the ‘excitation’ of optical spin because of the lack of *chiral impedance – which can only be obtained in hypothetical but unreal Tellegen media* [89]. Therefore, existing studies on SAM excitations in chiral materials inherently require loss to derive differentiated absorption of SAM modes during the propagation.

In this chapter, we report the excitation of SAM without any loss or magneto-optical effect by separating each optical spin in the spectral domain instead of applying selective annihilation or broken reciprocity. In a chiral resonant platform, we implement spin-dependent Fano resonances with ‘antisymmetric’ profiles, deriving the spectral separation of spins for the net excitation of SAM. For a deeper understanding of spin-dependent Fano resonance, we develop a temporal coupled mode analysis for chiral resonances for the first time, which demonstrates the origin of antisymmetric Fano resonances along the time axis. The conservative and nonmagnetic excitation of spin is achieved in our structure with great efficiency (excitation density of spin ± 1), compared with the previous record in circular dichroism (density ~ ± 0.5). Utilizing the extreme spectral sensitivity of spin-density reversal, we also propose ‘optical spin switching’ with experimentally accessible material parameters. Finally, as an

application, we propose ‘optical spin switching’ with experimentally accessible material parameters.

5.2 Optical Spin-Angular Momentum and Chiral Material

Optical spin angular momentum in relation to the handedness of photons [79] is a topic that has received significant attention. The excitation of optical SAM, or the generation of photons with a single handedness, is typically achieved with materials that have mirror symmetry, *i.e.*, optical chiral materials [80, 82, 90-96]. However, these materials are often limited in their selection in terms of accessible chiral parameters (wavevectors, impedances, losses) or chiral strength [92, 93].

Overcoming the restrictions in natural chiral materials, the field of optical chirality is now entering into a new regime, with the progress in fabrication technology. Artificially enhanced, designer chiral interactions [80, 82, 90, 91, 95, 97-99] using subwavelength structures have been demonstrated not only for fundamental interactions, such as spin-orbit coupling [100, 101], but also for a variety of applications, including enantiomer sensing [97, 99], negative refraction [86, 102, 103], and topological bandgaps [104, 105]. Approaches for notable artificial structures include nature-mimetic 3-

dimensional metamaterials of giant chirality [80, 82, 95, 102, 103] as well as 2-dimensional meta-films using the overlap of electric- and magnetic- dipoles [86, 90, 96] or non-Hermitian electric dipoles [106].

5.2.1 Theoretical background of circular birefringence

Although there are several version of constitutive relationships lead to the circular birefringence, for our purpose we follow the Tellegen form [92, 93]:

$$\begin{aligned} D &= \varepsilon E - i\chi H \\ B &= \mu H + i\chi E \end{aligned} \tag{5.1}$$

where χ represents the chirality properties. The wave vectors for each circular wave can be defined as $k_{\pm} = \omega\,((\mu\varepsilon)^{1/2} \pm \chi)$. Here "+" represents right-handed polarized (forward propagating), and left-handed polarized (backward propagating) circular wave; while "-"denotes left handed (forward propagating), and right-handed polarized (backward propagating) wave.

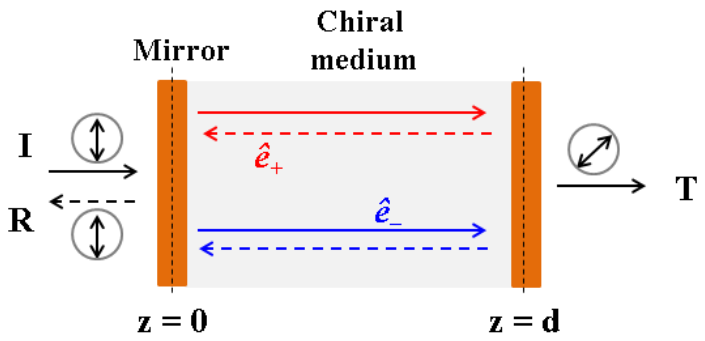

Figure 5.1 Natural rotation of a chiral resonator

Since chiral materials give different wavenumbers for a spin eigenvector propagating in opposite directions, for a resonator having for-/back- ward propagating mode at the same time, its chiral resonances cannot be analyzed easily and has not been treated within the frame of spin eigenvectors. As shown in Fig. 5.1 there is no accumulation of natural rotation during the back and forth resonant waves.

5.2.2 Optical SAM Excitation based on Spectral Separation

From the point of view of the excitation of optical SAM, nonetheless, it is noted that chiral materials alone do not establish sufficient conditions (Fig.5.2a).

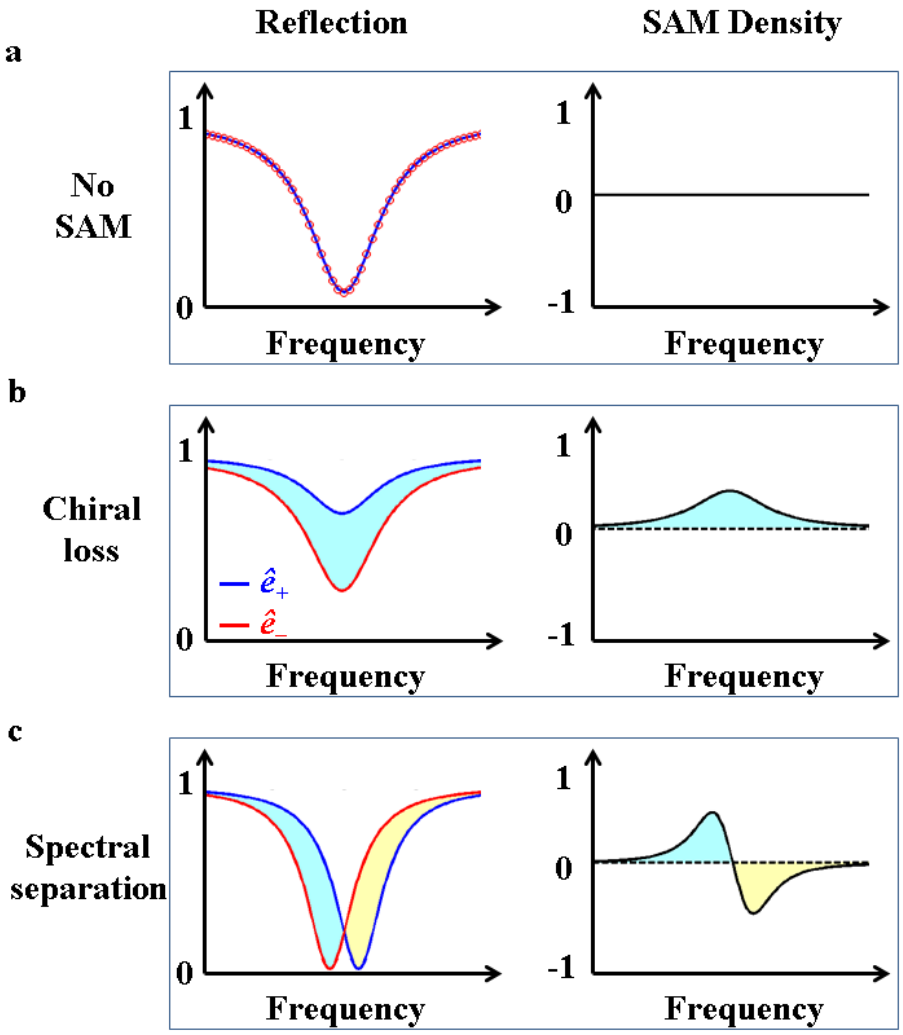

Figure 5.2 Reflection spectra and net SAM density from (a) chiral material, (b) circular dichroic material, and (c) spectral separation system. $\hat{e}_+$ (blue) and $\hat{e}_-$ (red) represent SAM of +1 and -1, respectively. The colored area (blue or yellow) indicate the same optical spin state.

Because of their *achiral impedance* (the absence of chiral impedance, having only spin-dependent wavevectors [92, 93]); in contrast to gyrotropic materials, which deliver nondegenerate chiral-*wavevectors* and *impedances* simultaneously [92, 107]. An alternative route toward SAM excitation in the absence of gyrotropic impedance can be made using circular dichroism [90, 92, 93, 96, 106, 108, 109] to selectively '*annihilate*' spins based on chiral *loss* (Fig.5.2b and Figure 5.2c), yet at the expense of inherent dissipation and the consequent degradation of the quality factor in the system. To achieve *conservative* and high-*Q* spin excitation with nonmagnetic materials, the spectral '*separation*' of spin can be envisaged (as in Figure 5.2c), yet has not been sought or demonstrated.

In the following section, we propose and demonstrate the nonmagnetic conservative excitation of optical SAM derived from the difference of two antisymmetric and spectrally separated Fano resonance spectra. Understanding that Fano resonances involve inherently asymmetric spectral profiles with shifted resonances [1, 3, 16, 17], it will be shown that, upon the opposite shift of Fano spectral pole for different handedness of photon, the spectral separation of spin and consequently the net excitation of SAM can be realized. As an implementation platform, we analyze a chiral resonator enclosed between a pair of identical linearly birefringent mirrors, which

provide different scattering pathways for the Fano interference.

5.2.3 Spectral Separation from Antisymmetric Fano Resonances

Figure 5.3a shows a schematic diagram of the proposed structure for Fano-resonant excitation of optical SAM. A Fabry-Perot resonator is constructed with a chiral material sandwiched between a pair of birefringent (ε_x, ε_y) mirrors, with neither chiral loss nor gyrotropic impedance. For comparison, Fig. 5.3b shows the reflection spectra of the resonator, with the highly birefringent film ($\varepsilon_x = \varepsilon_{metal} >> \varepsilon_y = \varepsilon_{dielec}$). In stark contrast to the case of $\varepsilon_x = \varepsilon_y$ (as shown in Fig. 5.4), the spectral separation of the $\hat{e}_{\pm}$ spin mode ($\hat{e}_{+}$ in blue and $\hat{e}_{-}$ in red) and the excitation of the net SAM (in blue and yellow area, in Fig. 5.3c) is evident.

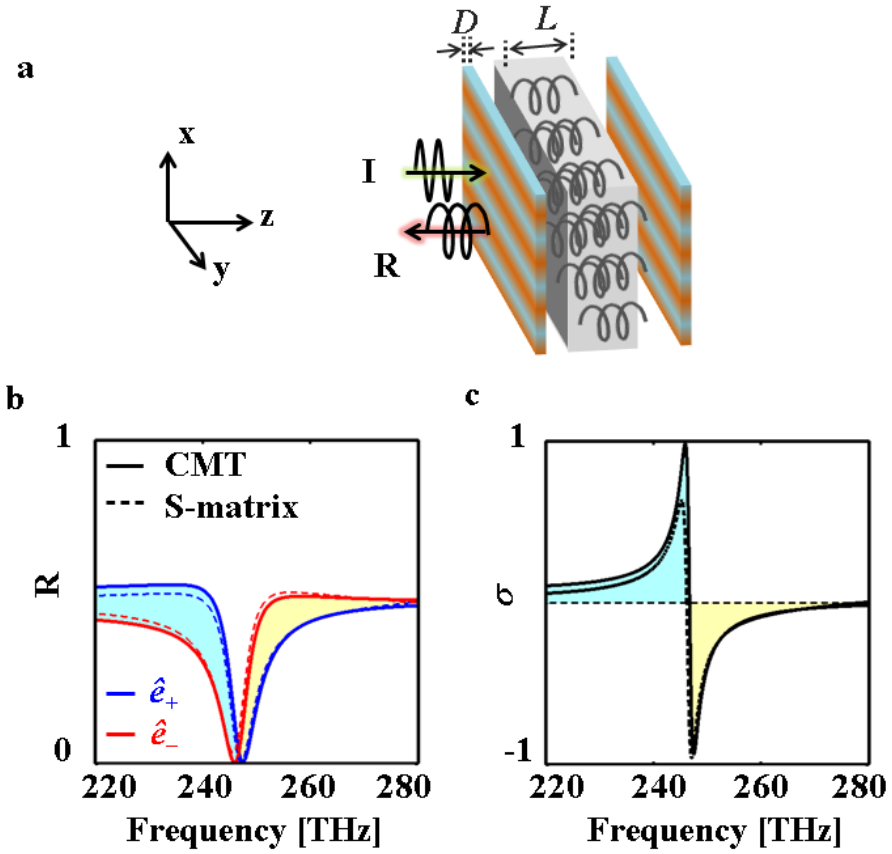

Figure 5.3 (a) Suggested chiral resonator (L = 350 nm, ε_{chiral} = 9, χ = 0.05) enclosed by highly birefringent mirrors (D = 20 nm, ε_x = ε_{metal} = -80, ε_y = ε_{dielec} = 2.25). (b) Reflection spectra of $\hat{e}_+$ (blue) and $\hat{e}_-$ (red) spin modes. (c) Spectra of SAM density σ (±1 denotes pure $\hat{e}_\pm$) with birefringent mirrors. The colored area (blue or yellow) indicates the same spin eigenvectors ($\hat{e}_+$ or $\hat{e}_-$)The calculations are based on both CMT (solid) and a scattering matrix (dashed).

Figure 5.3c shows the calculated spin density $\sigma = (R_{\hat{e}-} - R_{\hat{e}+}) / (R_{\hat{e}-} + R_{\hat{e}+})$, where $R_{\hat{e}\pm}$ is the reflectance of the $\hat{e}_{\pm}$ component, and $\sigma = \pm 1$ represents the pure spin state $\hat{e}_{\pm}$.. Compared with the case of circular dichroism ($\sigma \sim 0.5$) [108], a much larger spin density value $\sigma \sim 0.998$, close to the pure spin state, is achieved from the narrowband and antisymmetric Fano profiles.

For the special case of $\varepsilon_x = \varepsilon_y$, the response of the resonator calculated with CMT and a scattering matrix is shown in Fig. 5.3b and Fig. 5.3c (with $\varepsilon_{x,y} = \varepsilon_{metal} = -80$ and $\varepsilon_{x,y} = \varepsilon_{dielec} = 2.25$, assuming normal incidence of the *x*-polarized plane wave). With perfect overlap between the reflection spectra of the $\hat{e}_{\pm}$ spin modes based on CMT results and scattering matrix calculations, there is no spin excitation when $\varepsilon_x = \varepsilon_y$.

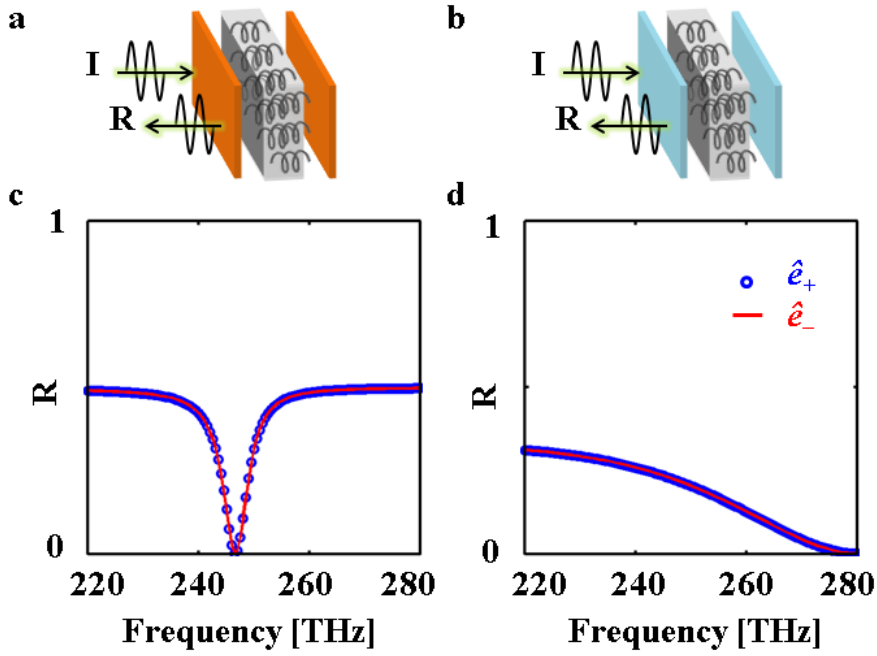

Figure 5.4 Schematics and reflection spectra of $\hat{e}_+$ (blue) and $\hat{e}_-$ (red) spin modes for special cases with homogeneous mirrors (a,c) metallic mirrors ($\varepsilon_x = \varepsilon_y = \varepsilon_{metal}$), and (b,d) dielectric mirrors ($\varepsilon_x = \varepsilon_y = \varepsilon_{dielec}$). The fitting values applied in CMT for the resonance (resonant frequency for the linear basis f_x = 246.66 THz and f_y = 142.7 THz) and the Q-factors (Q_x = 100 and Q_y = 12) for each mode (c and d) were obtained from the scattering matrix calculations.

Meanwhile it is clear that the emergence of Fano resonance for each spin state $\sigma = \pm 1$ is the result of the mixing between the narrowband (Fig. 5.2d) and broadband (Fig. 5.2d) scattering pathways, the underlying physics

of the opposite, antisymmetric shift of the Fano spectral pole in relation to the handedness of the spin needs to be further elaborated, as detailed in the later section.

5.3 Theoretical Modeling

By developing a temporal coupled mode theory [16, 17, 27, 28] for the Fano chiral resonator, we then prove that the handedness of the spin eigenvector is projected onto the temporal domain in the form of an opposite temporal shift, thereby leading to an antisymmetric Fano response in the spectral domain. An expression for the Fano parameter revealing its relation to the photon handedness and chirality is also derived and utilized in the quantitative control of spin excitation.

5.3.1 CMT Modeling in Temporal Domain

To investigate the origin of the spin-dependent antisymmetric Fano responses, we first need to develop a temporal CMT for chiral resonances. Considering the effect of natural optical rotation 2θ ($\theta = \omega \cdot \chi \cdot L_{eff} / 2c$, χ: unitless normalized value of material chirality, and L_{eff}: effective path, c: speed of light) [92, 93], we introduce the 'rotated' coordinates (h- and v-axes indicate the horizontal and vertical direction at the center of the chiral resonator, as shown

in Fig. 5.5a) for a chiral medium. The chiral resonant mode can then be decomposed into two linear resonant modes (a_h, a_v) orthogonal to each other and having modal decay times of τ_h and τ_v, respectively (Fig. 5.5a). Because the *h*- and *v*-axes are rotated by θ from the middle of the cavity to the mirror, we obtain $1 / \tau_h = \cos^2\theta / \tau_x + \sin^2\theta / \tau_y$ and $1 / \tau_v = \sin^2\theta / \tau_x + \cos^2\theta / \tau_y$, where τ_x and τ_y are the decay times for each birefringence axis, where we have $\tau_x \neq \tau_y$ when $\varepsilon_x \neq \varepsilon_y$. The CMT equation in *h*- and *v*- coordinates then becomes

$$\frac{d}{dt}\begin{bmatrix} a_h \\ a_v \end{bmatrix} = \begin{bmatrix} i\omega_{h0} - 2/\tau_h & 0 \\ 0 & i\omega_{v0} - 2/\tau_v \end{bmatrix} \cdot \begin{bmatrix} a_h \\ a_v \end{bmatrix}, \tag{5.1}$$

where ω_{h0} (or ω_{v0}) is the resonant frequency of the a_h (or a_v) mode.

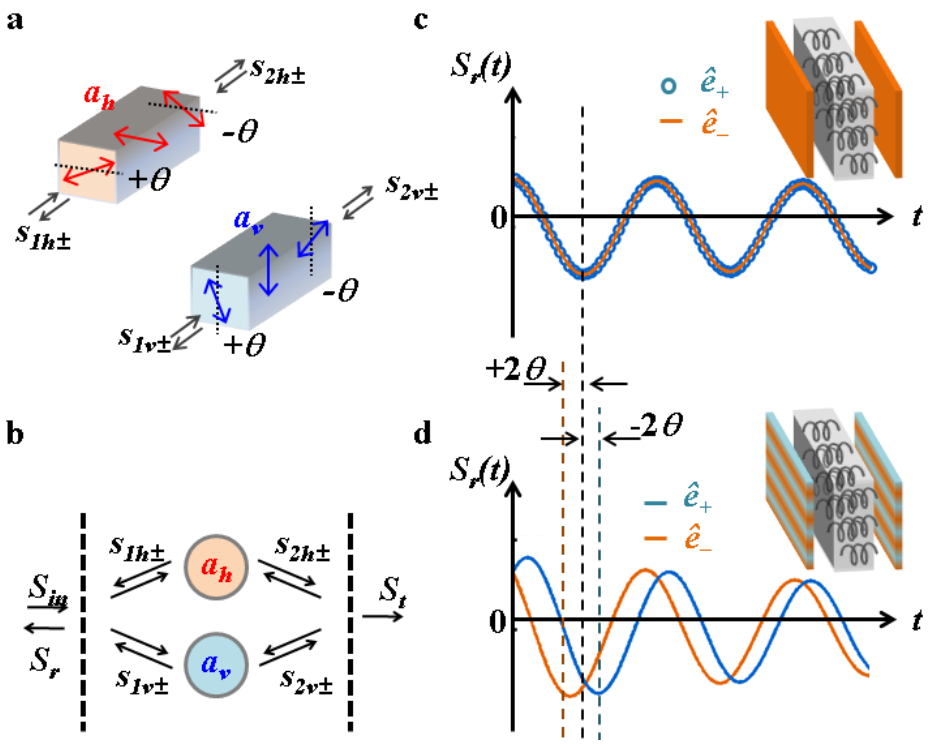

Figure 5.5 (a) Representation of a chiral resonator in linear basis *h* and *v* including natural optical rotation (horizontal and vertical in the middle of the resonator and rotated by $\pm\theta$ at the two interfaces). $S_{1(2)h(v)\pm}$ denotes the respective polarization component of incidence at the interface. (b) The CMT model of the chiral resonator with birefringent mirror set (as illustrated in Fig. 5.3a), with S_{in}: incidence, S_r: reflection, and S_t: transmission. Impulse $S_{1x}^{in} = \delta(t)$ response of the resonator for different spins ($\hat{e}_+$: blue, $\hat{e}_-$: red), with (c) $\varepsilon_x = \varepsilon_y = \varepsilon_{metal}$ and (d) $\varepsilon_x=\varepsilon_{metal}$, $\varepsilon_y=\varepsilon_{dielec}$. The dashed lines indicate temporal phase shifts of $\mp 2\theta$, obtained for $\hat{e}_\pm$, respectively. All of the results are calculated using the temporal CMT equation (Eq. (5.3)).

Upon the incident of *x*- and *y*-polarized waves (S_{1x+}, S_{1y+}) to the resonator (Fig. 5.3b), their couplings to resonance modes (a_h, a_v) can be written as

$$\frac{d}{dt}\begin{bmatrix} a_h \\ a_v \end{bmatrix} = \begin{bmatrix} i\omega_{h0} - 2/\tau_h & 0 \\ 0 & i\omega_{v0} - 2/\tau_v \end{bmatrix}\begin{bmatrix} a_h \\ a_v \end{bmatrix} + \begin{bmatrix} \kappa_h & 0 \\ 0 & \kappa_v \end{bmatrix} U_r \begin{bmatrix} S_{1x}^{\ in} \\ S_{1y}^{\ in} \end{bmatrix}, \quad (5.2)$$

For clearer analysis of the spin excitation, it is convenient to use a representation of Eq. (5.2) based on spin basis. Taking the spin form of $a_{\pm} = a_h \mp i a_v$ and $S_{1\pm}^{\ in} = S_{1x}^{\ in} \mp S_{1y}^{\ in}$, we then achieve the spin-form CMT upon the incident wave of $\boldsymbol{S}_{in} = [S_{1+}^{\ in}; S_{1-}^{\ in}]$ as follows:

$$\frac{d}{dt}\begin{bmatrix} a_+ \\ a_- \end{bmatrix} = i\begin{bmatrix} \omega_s & \omega_d \\ \omega_d & \omega_s \end{bmatrix}\begin{bmatrix} a_+ \\ a_- \end{bmatrix} + \begin{bmatrix} \kappa_s e^{-i\theta} & \kappa_d e^{i\theta} \\ \kappa_d e^{-i\theta} & \kappa_s e^{i\theta} \end{bmatrix}\vec{S}_{in}, \quad (5.3)$$

where $\omega_s = (\omega_{h0} + \omega_{v0})/2 + i\cdot(1/\tau_h + 1/\tau_v)$, $\omega_d = (\omega_{h0} - \omega_{v0})/2 + i\cdot(1/\tau_h - 1/\tau_v)$, $\kappa_s = (\kappa_h + \kappa_v)/2$, and $\kappa_d = (\kappa_h - \kappa_v)/2$. We emphasize that this spin-form CMT (Eq. (5.3)) clearly reveals the underlying physics of the spin-dependent Fano responses. First, mixing between spin modes a_+ and a_- through ω_d and κ_d occurs when $\tau_x \neq \tau_y$ (with the birefringent mirror case), breaking the spectral degeneracy of the spin modes. Second, as observed in the second

term of RHS, the incident waves undergo phase evolutions through $\kappa_s e^{\pm i\theta}$, in opposite directions for $\hat{e}_+$ and $\hat{e}_-$ spins, thus deriving the antisymmetric Fano response for opposite spins.

The temporal interpretation of Fano dynamics [15], based on the impulse response of Eq. (5.3) with $S_{1x}^{in} = \delta(t)$ further elucidates the origin of antisymmetric Fano resonances for opposite spin states. Figures 5.5c and 5.5d show the impulse responses of the chiral resonators having isotropic and birefringence mirrors, respectively. The temporal phase shift corresponding to Fano resonance [15], especially in the opposite direction for the $\hat{e}_+$ and $\hat{e}_-$ spin modes, exposes only when both conditions of $\theta \neq 0$ and $\tau_h \neq \tau_v$ are met at the same time. In detail, the phase shift for each spin ($\hat{e}_+$ and $\hat{e}_-$) takes the form of time-leading and lagging of $\pm 2\theta$ from the different scattering paths $\kappa_d e^{\pm i\theta}$ (in RHS of Eq. (5.3)). In the spectral representation, these temporal shifts correspond to shifts in the Fano resonant poles [15] in opposite directions and thus lead to two antisymmetric and spectrally separated Fano resonance spectra (Fig. 5.3b).

5.3.2 Derivation of Fano Asymmetry Parameter

Upon revealing the physics behind the SAM excitation based on antisymmetric Fano resonances, we now examine the key parameters for the

control of spin excitation in detail. To quantitatively assess the behavior of the system, by following the known definition of the Fano parameter [1, 16, 17], we define a complex-form Fano parameter q_s as the ratio of indirect-excitation to direct-excitation of the resonator, in this case $\kappa_d e^{i\theta}$ and $\kappa_s e^{-i\theta}$ (Eq. (5.3)). Then, we obtain

$$q_s = \frac{\kappa_d}{\kappa_s} e^{i2\theta}. \tag{5.4}$$

Figure 5.6 presents the SAM excitation spectra as a function of the argument $arg(q_s) = 2\theta$ and modulus $|q_s| = \kappa_d/\kappa_s$ of the Fano parameter. As observed in Fig. 5.6a, the bandwidth of the spin density σ decreases for smaller $arg(q_s) = 2\theta$, which is associated with the smaller spectral separations between the $\hat{e}_+$ and $\hat{e}_-$ modes (as in Fig. 5.6b).

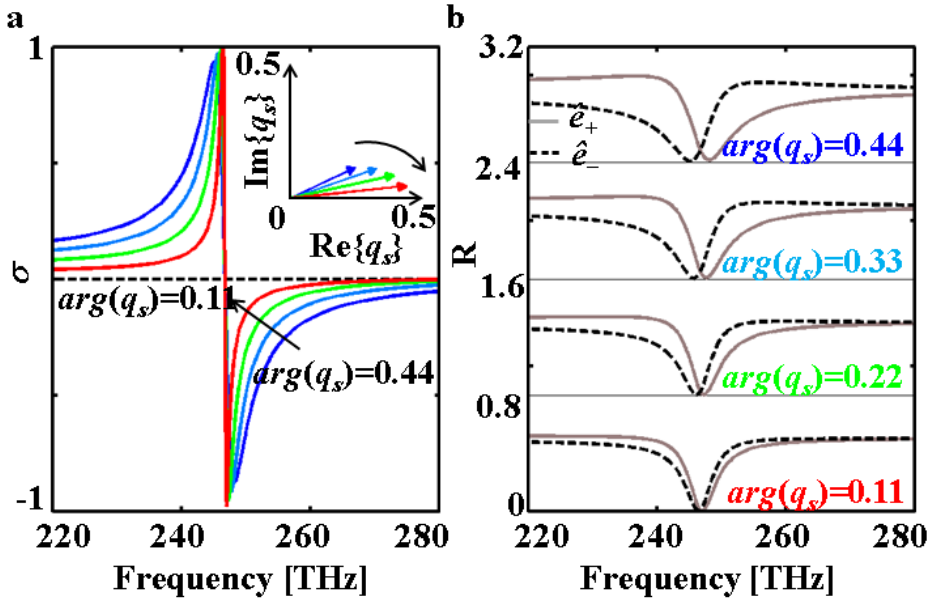

Figure 5.6 (a) Optical spin angular momentum density (σ) and (b) reflection (R) spectra as a function of $arg(q_s)$ = 0.44 to 0.11. In (b), the $\hat{e}_+$ (solid) and $\hat{e}_-$ (dashed) lines represent the states of σ = +1 and -1, respectively.

The spin excitation dependency on $|q_s|$ is also plotted in Fig. 5.7a, showing a smaller bandwidth of σ for larger $|q_s|$, which is again associated with the decrease in the spectral separation between the $\hat{e}_+$ and $\hat{e}_-$ modes (Fig. 5.7b).

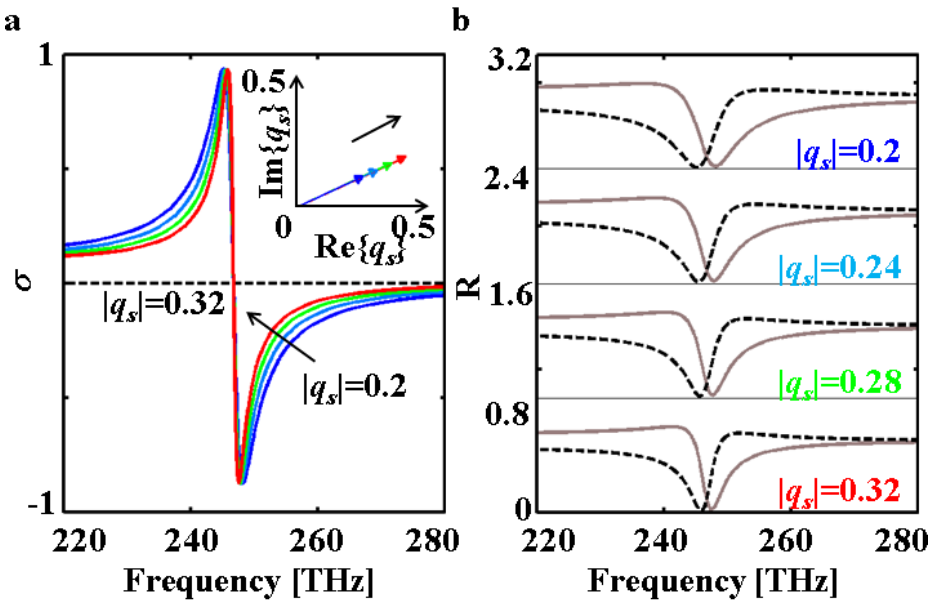

Figure 5.7 (a) Optical spin angular momentum density (σ) and (b) reflection (R) spectra as a function of $|q_s|$ = 0.2 to 0.32. In (b), the $\hat{e}_+$ (solid) and $\hat{e}_-$ (dashed) lines represent the states of σ = +1 and -1, respectively.

5.4 Optical Spin Switching

Utilizing the extreme spectral sensitivity of the spin-density σ, reversing its sign from +1 to -1 within $\Delta f \sim 1$ THz (Fig. 5.8), we demonstrate '*optical spin switching*', for the first time to our knowledge. Because the bandwidth of σ has a much stronger dependency on $arg(q_s)$ than $|q_s|$ and considering the practical limitation in the Q factor (Q = 550 for $|q_s| = \kappa_d / \kappa_s = 0.32$), we

assume spin switching based on the control of $arg(q_s)$, or equivalently ~ $\chi \cdot L_{eff}$. Figure 5.8a shows the schematics of the device, which has two electrodes connected to the chiral medium for the control of L_{eff} via refractive index tuning (e.g., Δn ~ 0.008 can be achieved with an ~ 1 V bias voltage [110-112]).

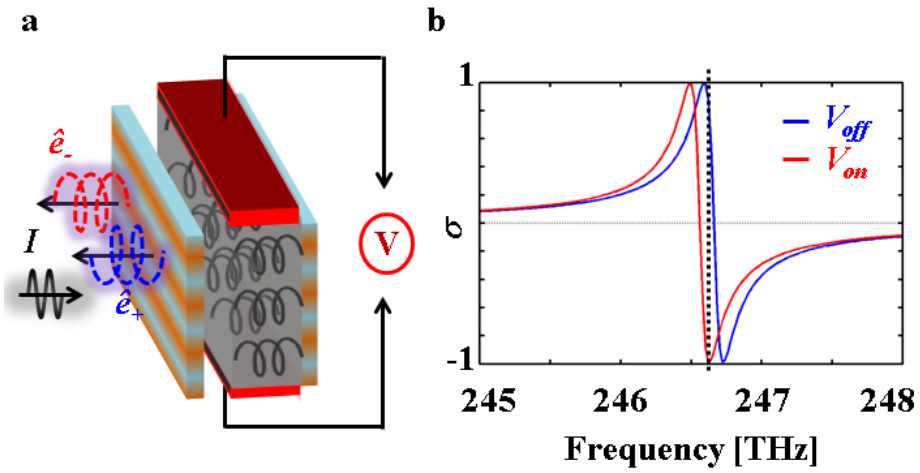

Figure 5.8 (a) Schematics of the optical spin switching. (b) SAM spectra without (blue, V_{off}) and with electric pumping (red, V_{on}, Δn = 0.001). Spin reversal from σ = 0.998 (blue) to σ = -0.993 (red) is observed from the application of the bias at the frequency 246.66 THz. All of the geometrical parameters are the same as those in Figure 5.3a, except for χ = 0.005.

For the case of electrical tuning of $\Delta n = 10^{-3}$, in Fig. 5.8b we show the consequent shift of the spin density spectra, which derives a sharp transition in σ from σ = 0.998 (black) to σ = -0.993 (red) at the working frequency of f

= 246.66 THz and with the value of normalized chirality χ = 0.005.

As shown in Fig. 5.9, even smaller values of χ (= 10^{-1} to 10^{-4}) and smaller tuning of Δn (10^{-2} to 10^{-5}) for spin switching is also possible but at the expense of a reduction in reflectance (0.4 to 10^{-4}).

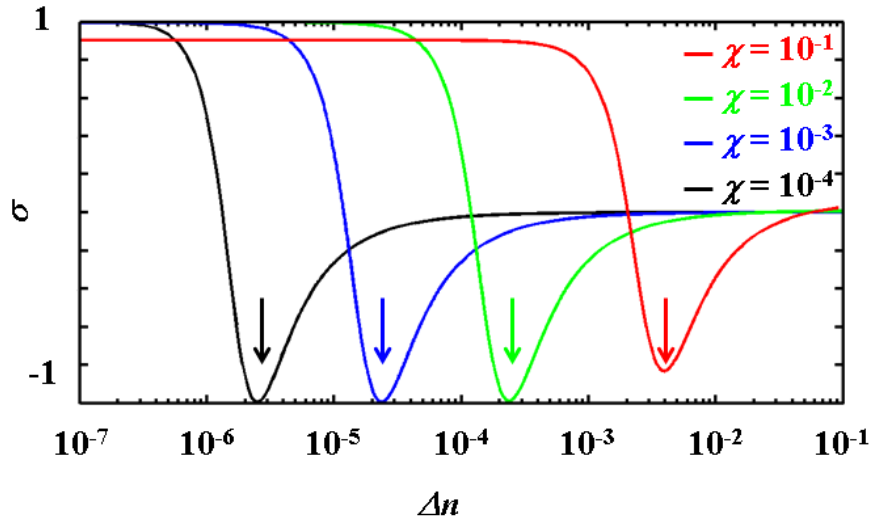

Figure 5.9 The spin density as a function of chirality χ (10^{-1} to 10^{-4}) and applied Δn (10^{-2} to 10^{-7}). The magnitude of Δn required for the SAM reversal for each value of χ is marked with arrows.

To achieve larger signal strength, artificially enhanced chiral metamaterials χ, where in [80, 82, 95, 108] there are χ > 0.005, combined with background materials with larger Δn (e.g., Δn >10^{-3} in liquid crystals,

Δn_{max} ~ 10^{-2} with Si [112], and even Δn_{max} ~ 1 with ITO [110], or by utilizing optical Kerr effect with optical pump with Δn_{max} ~ 10^{-3} with AlGaAs [111].) could be used with a minor penalty in the purity of the spin density (as shown in Fig. 5.10).

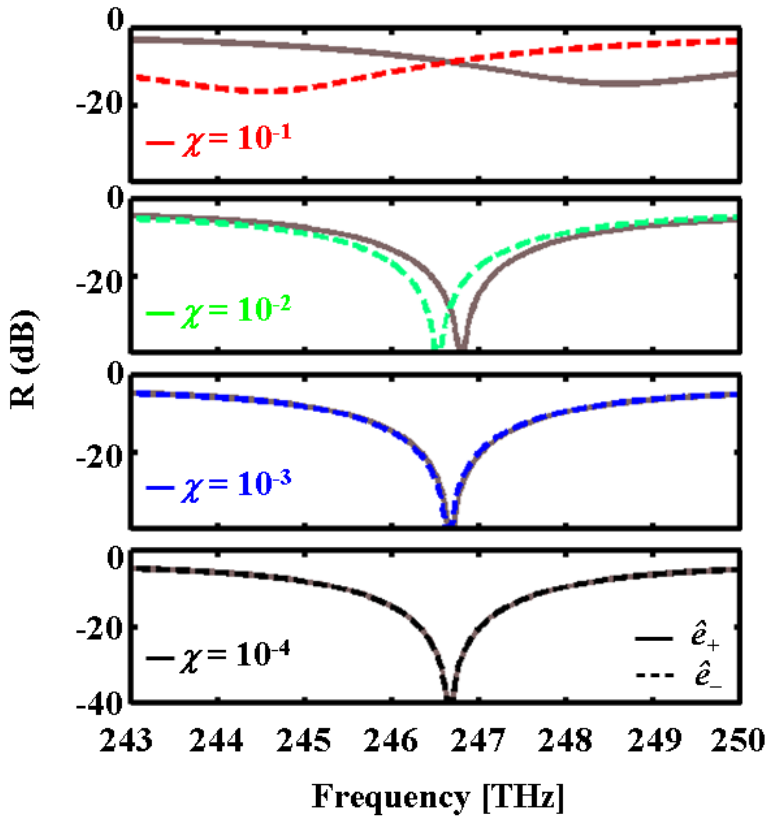

Figure 5.10 Reflectance spectra (R) for $\hat{e}_+$ (solid) and $\hat{e}_-$ (dashed) lines at each value of chirality χ (10^{-1} to 10^{-4}) and required Δn (10^{-2} to 10^{-7}).

5.5 Summary

In this chapter, we propose a new pathway for the nonmagnetic excitation of optical spin angular momentum based on the spin-dependent separation of Fano resonance spectra. By developing a spin-form temporal CMT for the chiral resonator, we unveil the origin of the spin-dependent antisymmetric Fano resonance in perfect agreement with the scattering matrix calculations. A complex Fano asymmetry parameter is derived to quantitatively control the spin excitation. 'Optical spin switching' is proposed for the first time, with experimentally accessible parameter values. Our results pave the way to nonmagnetic spin excitation and manipulation with high-Q response and Hermiticity without material chiral loss**.**

Chapter 6

Conclusion

6.1 Summary

In this dissertation, I explored Fano resonances in various platforms of optics and plasmonics. My researches were focused on 3 questions: “What is the origin of Fano resonance?”, “What is the best platform for strong Fano resonances?”, and “How can we use the results?”

Firstly we examined Fano resonances in plasmonic waveguide platforms. Based on its evanescent modes, plasmonic structures composed of interfaced metal and dielectric provide plentiful localized optical modes, which are the prerequisite of Fano resonances. We emphasized this feature

with a simple waveguide-stub structure, demonstrating that even in the subwavelength junction structure plasmonic resonances allow drastic and controllable Fano resonance, in sharp contrast to the case of PEC structure lacking local modes. Extending this fundamental result, we also achieved the Fano-resonant electromagnetically-induced transparency, from the participation of dark and bright plasmonic modes in a pair of stubs. Our results, supported by the single-parameter quantification based on the generalized coupled mode theory, enabled the most fundamental element for plasmonic integrated circuit: transmitting- / reflecting- plasmonic switching with superior performance.

In optical domain, we investigated Fano resonances in the polarization domain. Based on the interaction between different eigensystems, we achieved the interaction between optical spin angular momentum, deriving the spin-dependent separation of Fano resonance spectra. We also realized the quantification for these antisymmetric Fano responses successfully, newly-developing a spin-form temporal coupled mode theory. Such a spin-based Fano with a novel example of ‘optical spin switching’ will open a path to the high-Q spin excitation and manipulation of light without any assistance of material chiral loss or magnetic response.

6.2 Outlook

Our generalized analysis shows that two physical quantities are the participants of Fano resonances: coupling and bandwidth. Fano resonance is thus the universal phenomenon which occurs in certain interactions between resonances. In this context, in the field of Fano resonances, researches have focused on the utilization of many novel notions and structures in optics, to achieve strong, unconventional, and interdisciplinary forms of Fano resonances.

For example, the notion of parity-time symmetry satisfies the requirement for Fano resonances [106, 113, 114]. Due to its non-conservative nature, the elements inside parity-time symmetry usually support different bandwidth. More importantly, the non-orthogonality in non-Hermitian potentials inherently derives the coupling between optical elements. Due to its asymmetric and low-dimensional natures, parity-time symmetric potentials will provide novel physics of Fano resonances.

The structure with diverse k components also allows different scattering paths toward spectral domain. Therefore, random-walk potentials [115], deep-subwavelength potentials [116-118], or high-k potentials [119] will become a candidate for strong Fano resonances, because of their diverse k components. Such an approach in momentum k-space can also be linked

with our work in spin-angular momentum space [106], and also be extended to orbital-angular momentum space.

The quantum effect incorporated with sub-nm scaled structures has also attracted much attention in plasmonics. Due to its tunability based on the strength of electron-electron interactions, we can expect Fano-resonant behaviors between photonic and electronic states: corresponding to the interference between boson and fermion [120, 121]. I believe this new type of Fano resonances will be the bridge between photonics and electronics with high-*Q* response.

Journal Publications by the Author

(1) **X. Piao** *et al.* "Optical spin excitation based on antisymmetric Fano resonances", under review (2015).

(2) S. Yu, **X. Piao** *et al.* "Bloch-like wave dynamics in random-walk potentials based on supersymmetry", in revision (2015).

(3) S. Yu[†], **X. Piao**[†] *et al.* "Toward High-Q Perfect Absorption: A Fano Anti-laser", in revision (2015).

(4) S. Yu, **X. Piao** *et al.* "Unidirectional transition of optical modes based on causality in potential momentum space", under review (2015).

(5) S. Yu[†], H. S. Park[†], **X. Piao** *et al.* "Chiral interactions of light induced by low-dimensional dynamics in complex potentials", under review (2015).

(6) H. Kollmann, **X. Piao** *et al.* "Towards Plasmonics with Nanometer Precision: Nonlinear Optics of Helium-Ion Milled Gold Nanoantennas", Nano Lett. **14**, 4778 (2014).

(7) S. Yu, D. R. Mason, **X. Piao** et al. "Phase-Dependent Reversible Non-reciprocity in Complex Meta-molecules", Phys. Rev. B **87**, 125143 (2013).

(8) X. Chen, H. Park, M. Pelton, **X. Piao** et al. “Atomic Layer Lithography of Wafer-Scale Nanogap Arrays for Extreme Confinement of Electromagnetic Waves”, Nature Commun. **4**, 2361 (2013).

(9) S. Yu, **X. Piao** et al. “Spatiospectral Separation of Exceptional Points in PT-Symmetric Optical Potentials”, Phys. Rev. A **86**, 031802 (2012)

(10) **X. Piao**, S. Yu, and N. Park, “Control of Fano Asymmetry in Plasmon Induced Transparency and its Application to Plasmonic Waveguide Modulator”, Opt. Express **20**, 18994 (2012)

(11) S. Yu, **X. Piao**, and N. Park, “Slow-Light Dispersion Properties of Multiatomic Multiband Coupled Resonator Optical Waveguides”, Phys. Rev. A **85**, 023823 (2012).

(12) S. Yu, **X. Piao** et al. “Mode Junction Photonics with a Symmetry-Breaking Arrangement of Mode-Orthogonal Heterostructures”, Opt. Express **19**, 25500 (2011).

(13) **X. Piao** et al. “Fano-Type Spectral Asymmetry and its Control for Plasmonic Metal-Insulator-Metal Stub Structures”, Opt. Express **19**, 10907 (2011).

(14) M. S. Kumar, **X. Piao** et al. “Out of Plane Mode Conversion and Manipulation of Surface Plasmon Polariton Waves”, Opt. Express **18**, 8800 (2010).

Bibliography

[1] U. Fano, "Effects of configuration interaction on intensities and phase shifts," *Physical Review,* vol. 124, p. 1866, 1961.

[2] U. Fano, "On the absorption spectrum of noble gases at the arc spectrum limit," *arXiv preprint cond-mat/0502210,* 2005.

[3] B. Luk'yanchuk, N. I. Zheludev, S. A. Maier, N. J. Halas, P. Nordlander, H. Giessen, *et al.*, "The Fano resonance in plasmonic nanostructures and metamaterials," *Nature materials,* vol. 9, pp. 707-715, 2010.

[4] A. E. Miroshnichenko, S. Flach, and Y. S. Kivshar, "Fano resonances in nanoscale structures," *Reviews of Modern Physics,* vol. 82, p. 2257, 2010.

[5] A. B. Khanikaev, C. Wu, and G. Shvets, "Fano-resonant metamaterials and their applications," *Nanophotonics,* vol. 2, pp. 247-264, 2013.

[6] Y. Yang, I. I. Kravchenko, D. P. Briggs, and J. Valentine, "All-dielectric metasurface analogue of electromagnetically induced transparency," *Nature communications,* vol. 5, 2014.

[7] C. Wu, A. B. Khanikaev, and G. Shvets, "Broadband slow light metamaterial based on a double-continuum Fano resonance," *Physical review letters,* vol. 106, p. 107403, 2011.

[8] S. N. Sheikholeslami, A. García-Etxarri, and J. A. Dionne,

"Controlling the interplay of electric and magnetic modes via Fano-like plasmon resonances," *Nano letters,* vol. 11, pp. 3927-3934, 2011.

[9] A. Artar, A. A. Yanik, and H. Altug, "Directional double Fano resonances in plasmonic hetero-oligomers," *Nano letters,* vol. 11, pp. 3694-3700, 2011.

[10] M. V. Rybin, P. V. Kapitanova, D. S. Filonov, A. P. Slobozhanyuk, P. A. Belov, Y. S. Kivshar*, et al.*, "Fano resonances in antennas: General control over radiation patterns," *Physical Review B,* vol. 88, p. 205106, 2013.

[11] C. Wu, A. B. Khanikaev, R. Adato, N. Arju, A. A. Yanik, H. Altug*, et al.*, "Fano-resonant asymmetric metamaterials for ultrasensitive spectroscopy and identification of molecular monolayers," *Nature materials,* vol. 11, pp. 69-75, 2012.

[12] P. Fan, Z. Yu, S. Fan, and M. L. Brongersma, "Optical Fano resonance of an individual semiconductor nanostructure," *Nature materials,* 2014.

[13] C. Wu, N. Arju, G. Kelp, J. A. Fan, J. Dominguez, E. Gonzales*, et al.*, "Spectrally selective chiral silicon metasurfaces based on infrared Fano resonances," *Nature communications,* vol. 5, 2014.

[14] F. Shafiei, F. Monticone, K. Q. Le, X.-X. Liu, T. Hartsfield, A. Alù*, et al.*, "A subwavelength plasmonic metamolecule exhibiting magnetic-based optical Fano resonance," *Nature nanotechnology,* vol. 8, pp. 95-99, 2013.

[15] C. Ott, A. Kaldun, P. Raith, K. Meyer, M. Laux, J. Evers*, et al.*, "Lorentz meets Fano in spectral line shapes: A universal phase and its laser control," *Science,* vol. 340, pp. 716-720, 2013.

[16] X. Piao, S. Yu, S. Koo, K. Lee, and N. Park, "Fano-type spectral asymmetry and its control for plasmonic metal-

insulator-metal stub structures," *Optics express,* vol. 19, pp. 10907-10912, 2011.

[17] X. Piao, S. Yu, and N. Park, "Control of Fano asymmetry in plasmon induced transparency and its application to plasmonic waveguide modulator," *Optics express,* vol. 20, pp. 18994-18999, 2012.

[18] I. Soboleva, V. Moskalenko, and A. Fedyanin, "Giant Goos-Hänchen Effect and Fano Resonance at Photonic Crystal Surfaces," *Physical review letters,* vol. 108, p. 123901, 2012.

[19] I. V. Shadrivov, A. A. Zharov, and Y. S. Kivshar, "Giant Goos-Hänchen effect at the reflection from left-handed metamaterials," *Applied Physics Letters,* vol. 83, pp. 2713-2715, 2003.

[20] X. Yin, L. Hesselink, Z. Liu, N. Fang, and X. Zhang, "Large positive and negative lateral optical beam displacements due to surface plasmon resonance," *Applied Physics Letters,* vol. 85, pp. 372-374, 2004.

[21] C. Bonnet, D. Chauvat, O. Emile, F. Bretenaker, A. Le Floch, and L. Dutriaux, "Measurement of positive and negative Goos--Hänchen effects for metallic gratings near Wood anomalies," *Optics letters,* vol. 26, pp. 666-668, 2001.

[22] V. Moskalenko, I. Soboleva, and A. Fedyanin, "Surface wave-induced enhancement of the Goos-Hänchen effect in one-dimensional photonic crystals," *JETP Letters,* vol. 91, pp. 382-386, 2010.

[23] Y. S. Joe, A. M. Satanin, and C. S. Kim, "Classical analogy of Fano resonances," *Physica Scripta,* vol. 74, p. 259, 2006.

[24] D. M. Riffe, "Classical fano oscillator," *Physical Review B,* vol. 84, p. 064308, 2011.

[25] S. Fan, "Sharp asymmetric line shapes in side-coupled

waveguide-cavity systems," *Applied Physics Letters,* vol. 80, pp. 908-910, 2002.

[26] S. Fan, W. Suh, and J. Joannopoulos, "Temporal coupled-mode theory for the Fano resonance in optical resonators," *JOSA A,* vol. 20, pp. 569-572, 2003.

[27] H. A. Haus, *Waves and fields in optoelectronics* vol. 464: Prentice-Hall Englewood Cliffs, NJ, 1984.

[28] J. D. Joannopoulos, S. G. Johnson, J. N. Winn, and R. D. Meade, *Photonic crystals: molding the flow of light*: Princeton university press, 2011.

[29] Q. Li, T. Wang, Y. Su, M. Yan, and M. Qiu, "Coupled mode theory analysis of mode-splitting in coupled cavity system," *Optics express,* vol. 18, pp. 8367-8382, 2010.

[30] B. Maes, P. Bienstman, and R. Baets, "Switching in coupled nonlinear photonic-crystal resonators," *JOSA B,* vol. 22, pp. 1778-1784, 2005.

[31] C. Manolatou, M. Khan, S. Fan, P. R. Villeneuve, H. Haus, and J. Joannopoulos, "Coupling of modes analysis of resonant channel add-drop filters," *Quantum Electronics, IEEE Journal of,* vol. 35, pp. 1322-1331, 1999.

[32] W. Suh, Z. Wang, and S. Fan, "Temporal coupled-mode theory and the presence of non-orthogonal modes in lossless multimode cavities," *Quantum Electronics, IEEE Journal of,* vol. 40, pp. 1511-1518, 2004.

[33] D. M. Pozar, *Microwave engineering*: John Wiley & Sons, 2009.

[34] Y. Matsuzaki, T. Okamoto, M. Haraguchi, M. Fukui, and M. Nakagaki, "Characteristics of gap plasmon waveguide with stub structures," *Optics express,* vol. 16, pp. 16314-16325, 2008.

[35] L. Yang, C. Min, and G. Veronis, "Guided subwavelength slow-

light mode supported by a plasmonic waveguide system," *Optics letters,* vol. 35, pp. 4184-4186, 2010.

[36] R. Stoffer, H. Hoekstra, R. De Ridder, E. Van Groesen, and F. Van Beckum, "Numerical studies of 2D photonic crystals: Waveguides, coupling between waveguides and filters," *Optical and Quantum Electronics,* vol. 32, pp. 947-961, 2000.

[37] Z. Han and S. I. Bozhevolnyi, "Plasmon-induced transparency with detuned ultracompact Fabry-Perot resonators in integrated plasmonic devices," *Optics express,* vol. 19, pp. 3251-3257, 2011.

[38] X.-S. Lin and X.-G. Huang, "Tooth-shaped plasmonic waveguide filters with nanometeric sizes," *Optics letters,* vol. 33, pp. 2874-2876, 2008.

[39] K. Ogusu and K. Takayama, "Transmission characteristics of photonic crystal waveguides with stubs and their application to optical filters," *Optics letters,* vol. 32, pp. 2185-2187, 2007.

[40] J. Tao, X. G. Huang, and J. H. Zhu, "A wavelength demultiplexing structure based on metal-dielectric-metal plasmonic nano-capillary resonators," *Optics express,* vol. 18, pp. 11111-11116, 2010.

[41] J. Tao, X. G. Huang, X. Lin, Q. Zhang, and X. Jin, "A narrow-band subwavelength plasmonic waveguide filter with asymmetrical multiple-teeth-shaped structure," *Optics express,* vol. 17, pp. 13989-13994, 2009.

[42] X. Lin and X. Huang, "Numerical modeling of a teeth-shaped nanoplasmonic waveguide filter," *JOSA B,* vol. 26, pp. 1263-1268, 2009.

[43] J. Tao, X. G. Huang, X. Lin, J. Chen, Q. Zhang, and X. Jin, "Systematical research on characteristics of double-sided teeth-shaped nanoplasmonic waveguide filters," *JOSA B,* vol.

27, pp. 323-327, 2010.

[44] C. Min and G. Veronis, "Absorption switches in metal-dielectric-metal plasmonic waveguides," *Optics Express,* vol. 17, pp. 10757-10766, 2009.

[45] A. A. Reiserer, J.-S. Huang, B. Hecht, and T. Brixner, "Subwavelength broadband splitters and switches for femtosecond plasmonic signals," *Optics express,* vol. 18, pp. 11810-11820, 2010.

[46] H. Lu, X. Liu, L. Wang, Y. Gong, and D. Mao, "Ultrafast all-optical switching in nanoplasmonic waveguide with Kerr nonlinear resonator," *Optics express,* vol. 19, pp. 2910-2915, 2011.

[47] A. Pannipitiya, I. D. Rukhlenko, M. Premaratne, H. T. Hattori, and G. P. Agrawal, "Improved transmission model for metal-dielectric-metal plasmonic waveguides with stub structure," *Optics express,* vol. 18, pp. 6191-6204, 2010.

[48] L. O. Diniz, F. D. Nunes, E. Marega, J. Weiner, and B.-H. V. Borges, "Metal–insulator–metal surface plasmon polariton waveguide filters with cascaded transverse cavities," *Journal of Lightwave Technology,* vol. 29, pp. 714-720, 2011.

[49] L. Diniz, F. Nunes, E. Marega Jr, and B.-H. Borges, "A novel subwavelength plasmon-polariton optical filter based on tilted coupled structures," *Applied Physics A,* vol. 103, pp. 649-652, 2011.

[50] J. Liu, G. Fang, H. Zhao, Y. Zhang, and S. Liu, "Surface plasmon reflector based on serial stub structure," *Optics express,* vol. 17, pp. 20134-20139, 2009.

[51] J. Wang, Y. Wang, X. Zhang, K. Yang, Y. Wang, S. Liu*, et al.*, "A transmission line model for subwavelength metallic grating with single cut," *Optik-International Journal for Light and*

Electron Optics, vol. 122, pp. 1808-1810, 2011.

[52] F. Wang, X. Wang, H. Zhou, Q. Zhou, Y. Hao, X. Jiang, *et al.*, "Fano-resonance-based Mach-Zehnder optical switch employing dual-bus coupled ring resonator as two-beam interferometer," *Optics express,* vol. 17, pp. 7708-7716, 2009.

[53] X. Yang, C. Husko, C. W. Wong, M. Yu, and D.-L. Kwong, "Observation of femtojoule optical bistability involving Fano resonances in high-Q/V m silicon photonic crystal nanocavities," *Applied Physics Letters,* vol. 91, pp. 051113-051113-3, 2007.

[54] Z.-J. Zhong, Y. Xu, S. Lan, Q.-F. Dai, and L.-J. Wu, "Sharp and asymmetric transmission response in metal-dielectric-metal plasmonic waveguides containing Kerr nonlinear media," *Optics express,* vol. 18, pp. 79-86, 2010.

[55] S. G. Johnson, C. Manolatou, S. Fan, P. R. Villeneuve, J. Joannopoulos, and H. Haus, "Elimination of cross talk in waveguide intersections," *Optics Letters,* vol. 23, pp. 1855-1857, 1998.

[56] S. Fan, S. G. Johnson, J. Joannopoulos, C. Manolatou, and H. Haus, "Waveguide branches in photonic crystals," *JOSA B,* vol. 18, pp. 162-165, 2001.

[57] K.-J. Boller, A. Imamolu, and S. E. Harris, "Observation of electromagnetically induced transparency," *Physical Review Letters,* vol. 66, p. 2593, 1991.

[58] A. Andre, M. Eisaman, R. Walsworth, A. Zibrov, and M. Lukin, "Quantum control of light using electromagnetically induced transparency," *Journal of Physics B: Atomic, Molecular and Optical Physics,* vol. 38, p. S589, 2005.

[59] A. H. Safavi-Naeini, T. M. Alegre, J. Chan, M. Eichenfield, M. Winger, Q. Lin, *et al.*, "Electromagnetically induced

transparency and slow light with optomechanics," *Nature,* vol. 472, pp. 69-73, 2011.

[60] A. Kasapi, M. Jain, G. Yin, and S. E. Harris, "Electromagnetically induced transparency: propagation dynamics," *Physical review letters,* vol. 74, p. 2447, 1995.

[61] S. Zhang, D. A. Genov, Y. Wang, M. Liu, and X. Zhang, "Plasmon-induced transparency in metamaterials," *Physical Review Letters,* vol. 101, p. 047401, 2008.

[62] C. G. Alzar, M. Martinez, and P. Nussenzveig, "Classical analog of electromagnetically induced transparency," *American Journal of Physics,* vol. 70, pp. 37-41, 2002.

[63] N. Liu, L. Langguth, T. Weiss, J. Kästel, M. Fleischhauer, T. Pfau, *et al.*, "Plasmonic analogue of electromagnetically induced transparency at the Drude damping limit," *Nature materials,* vol. 8, pp. 758-762, 2009.

[64] D. D. Smith, H. Chang, K. A. Fuller, A. Rosenberger, and R. W. Boyd, "Coupled-resonator-induced transparency," *Physical Review A,* vol. 69, p. 063804, 2004.

[65] R. D. Kekatpure, E. S. Barnard, W. Cai, and M. L. Brongersma, "Phase-coupled plasmon-induced transparency," *Physical review letters,* vol. 104, p. 243902, 2010.

[66] M. Tomita, K. Totsuka, R. Hanamura, and T. Matsumoto, "Tunable Fano interference effect in coupled-microsphere resonator-induced transparency," *JOSA B,* vol. 26, pp. 813-818, 2009.

[67] P. Tassin, L. Zhang, T. Koschny, E. Economou, and C. M. Soukoulis, "Low-loss metamaterials based on classical electromagnetically induced transparency," *Physical review letters,* vol. 102, p. 053901, 2009.

[68] A. E. Çetin, A. Artar, M. Turkmen, A. A. Yanik, and H. Altug,

"Plasmon induced transparency in cascaded π-shaped metamaterials," *Optics express,* vol. 19, pp. 22607-22618, 2011.

[69] Y. Huang, C. Min, and G. Veronis, "Subwavelength slow-light waveguides based on a plasmonic analogue of electromagnetically induced transparency," *Applied Physics Letters,* vol. 99, p. 143117, 2011.

[70] N. Papasimakis, Y. Fu, V. Fedotov, S. Prosvirnin, D. Tsai, and N. Zheludev, "Metamaterial with polarization and direction insensitive resonant transmission response mimicking electromagnetically induced transparency," *Applied Physics Letters,* vol. 94, p. 211902, 2009.

[71] H. Schmidt, K. Campman, A. Gossard, and A. Imamoğlu, "Tunneling induced transparency: Fano interference in intersubband transitions," *Applied physics letters,* vol. 70, pp. 3455-3457, 1997.

[72] V. Giannini, Y. Francescato, H. Amrania, C. C. Phillips, and S. A. Maier, "Fano resonances in nanoscale plasmonic systems: a parameter-free modeling approach," *Nano letters,* vol. 11, pp. 2835-2840, 2011.

[73] N. A. Mirin, K. Bao, and P. Nordlander, "Fano resonances in plasmonic nanoparticle aggregates†," *The Journal of Physical Chemistry A,* vol. 113, pp. 4028-4034, 2009.

[74] F. López-Tejeira, R. Paniagua-Domínguez, R. Rodríguez-Oliveros, and J. Sánchez-Gil, "Fano-like interference of plasmon resonances at a single rod-shaped nanoantenna," *New Journal of Physics,* vol. 14, p. 023035, 2012.

[75] C. Argyropoulos, P.-Y. Chen, F. Monticone, G. D'Aguanno, and A. Alu, "Nonlinear plasmonic cloaks to realize giant all-optical scattering switching," *Physical review letters,* vol. 108, p.

263905, 2012.

[76] Y. Francescato, V. Giannini, and S. A. Maier, "Plasmonic systems unveiled by Fano resonances," *ACS nano,* vol. 6, pp. 1830-1838, 2012.

[77] W. Cai, J. S. White, and M. L. Brongersma, "Compact, high-speed and power-efficient electrooptic plasmonic modulators," *Nano Letters,* vol. 9, pp. 4403-4411, 2009.

[78] P. B. Johnson and R.-W. Christy, "Optical constants of the noble metals," *Physical Review B,* vol. 6, p. 4370, 1972.

[79] S. Van Enk and G. Nienhuis, "Spin and orbital angular momentum of photons," *EPL (Europhysics Letters),* vol. 25, p. 497, 1994.

[80] M. Thiel, M. S. Rill, G. von Freymann, and M. Wegener, "Three-Dimensional Bi-Chiral Photonic Crystals," *Advanced Materials,* vol. 21, pp. 4680-4682, 2009.

[81] M. Thiel, H. Fischer, G. Von Freymann, and M. Wegener, "Three-dimensional chiral photonic superlattices," *Optics letters,* vol. 35, pp. 166-168, 2010.

[82] Y. Zhao, M. Belkin, and A. Alù, "Twisted optical metamaterials for planarized ultrathin broadband circular polarizers," *Nature communications,* vol. 3, p. 870, 2012.

[83] B. Frank, X. Yin, M. Scha¨ferling, J. Zhao, S. M. Hein, P. V. Braun*, et al.*, "Large-area 3D chiral plasmonic structures," *ACS nano,* vol. 7, pp. 6321-6329, 2013.

[84] V. Agranovich, Y. N. Gartstein, and A. Zakhidov, "Negative refraction in gyrotropic media," *Physical Review B,* vol. 73, p. 045114, 2006.

[85] M. Schäferling, D. Dregely, M. Hentschel, and H. Giessen, "Tailoring enhanced optical chirality: design principles for chiral plasmonic nanostructures," *Physical Review X,* vol. 2, p.

031010, 2012.

[86] E. Plum, J. Zhou, J. Dong, V. Fedotov, T. Koschny, C. Soukoulis, *et al.*, "Metamaterial with negative index due to chirality," *Physical Review B,* vol. 79, p. 035407, 2009.

[87] E. Plum, X.-X. Liu, V. Fedotov, Y. Chen, D. Tsai, and N. Zheludev, "Metamaterials: optical activity without chirality," *Physical review letters,* vol. 102, p. 113902, 2009.

[88] S. H. Mousavi, A. B. Khanikaev, J. Allen, M. Allen, and G. Shvets, "Gyromagnetically induced transparency of metasurfaces," *Physical review letters,* vol. 112, p. 117402, 2014.

[89] S. Tretyakov, S. Maslovski, I. Nefedov, A. Viitanen, P. Belov, and A. Sanmartin, "Artificial tellegen particle," *Electromagnetics,* vol. 23, pp. 665-680, 2003.

[90] V. Fedotov, P. Mladyonov, S. Prosvirnin, A. Rogacheva, Y. Chen, and N. Zheludev, "Asymmetric propagation of electromagnetic waves through a planar chiral structure," *Physical review letters,* vol. 97, p. 167401, 2006.

[91] S. Chen, D. Katsis, A. Schmid, J. Mastrangelo, T. Tsutsui, and T. Blanton, "Circularly polarized light generated by photoexcitation of luminophores in glassy liquid-crystal films," *Nature,* vol. 397, pp. 506-508, 1999.

[92] S. J. Orfanidis, *Electromagnetic waves and antennas*: Rutgers University New Brunswick, NJ, 2002.

[93] A. Serdyukov, I. Semchenko, S. Tretyakov, and A. Sihvola, "Electromagnetics of bi-anisotropic materials:{T} heory and applications," 2001.

[94] S. Furumi and N. Tamaoki, "Glass-Forming Cholesteric Liquid Crystal Oligomers for New Tunable Solid-State Laser," *Advanced Materials,* vol. 22, pp. 886-891, 2010.

[95] J. K. Gansel, M. Thiel, M. S. Rill, M. Decker, K. Bade, V. Saile, *et al.*, "Gold helix photonic metamaterial as broadband circular polarizer," *Science,* vol. 325, pp. 1513-1515, 2009.

[96] Z. Li, M. Gokkavas, and E. Ozbay, "Manipulation of asymmetric transmission in planar chiral nanostructures by anisotropic loss," *Advanced Optical Materials,* vol. 1, pp. 482-488, 2013.

[97] Y. Tang and A. E. Cohen, "Enhanced enantioselectivity in excitation of chiral molecules by superchiral light," *Science,* vol. 332, pp. 333-336, 2011.

[98] E. Saenz, I. Semchenko, S. Khakhomov, K. Guven, R. Gonzalo, E. Ozbay, *et al.*, "Modeling of spirals with equal dielectric, magnetic, and chiral susceptibilities," *Electromagnetics,* vol. 28, pp. 476-493, 2008.

[99] Y. Tang and A. E. Cohen, "Optical chirality and its interaction with matter," *Physical review letters,* vol. 104, p. 163901, 2010.

[100] A. Asenjo-Garcia and F. G. de Abajo, "Dichroism in the Interaction between Vortex Electron Beams, Plasmons, and Molecules," *Physical review letters,* vol. 113, p. 066102, 2014.

[101] E. Brasselet, Y. Izdebskaya, V. Shvedov, A. S. Desyatnikov, W. Krolikowski, and Y. S. Kivshar, "Dynamics of optical spin-orbit coupling in uniaxial crystals," *Optics letters,* vol. 34, pp. 1021-1023, 2009.

[102] J. Pendry, "A chiral route to negative refraction," *Science,* vol. 306, pp. 1353-1355, 2004.

[103] S. Zhang, Y.-S. Park, J. Li, X. Lu, W. Zhang, and X. Zhang, "Negative refractive index in chiral metamaterials," *Physical review letters,* vol. 102, p. 023901, 2009.

[104] M. C. Rechtsman, J. M. Zeuner, Y. Plotnik, Y. Lumer, D. Podolsky, F. Dreisow, *et al.*, "Photonic Floquet topological

insulators," *Nature,* vol. 496, pp. 196-200, 2013.

[105] A. B. Khanikaev, S. H. Mousavi, W.-K. Tse, M. Kargarian, A. H. MacDonald, and G. Shvets, "Photonic topological insulators," *Nature materials,* vol. 12, pp. 233-239, 2013.

[106] S. Yu, H. S. Park, X. Piao, B. Min, and N. Park, "Chiral interactions of light induced by low-dimensional dynamics in complex potentials," *arXiv preprint arXiv:1409.0180,* 2014.

[107] D. Martin, K. Neal, and T. Dean, "The optical and magneto-optical behaviour of ferromagnetic metals," *Proceedings of the Physical Society,* vol. 86, p. 605, 1965.

[108] S. Droulias and V. Yannopapas, "Broad-band giant circular dichroism in metamaterials of twisted chains of metallic nanoparticles," *The Journal of Physical Chemistry C,* vol. 117, pp. 1130-1135, 2013.

[109] T. Cao, G. Wang, W. Han, H. Ye, C. Zhu, J. Shi*, et al.*, "Valley-selective circular dichroism of monolayer molybdenum disulphide," *Nature communications,* vol. 3, p. 887, 2012.

[110] H. W. Lee, G. Papadakis, S. P. Burgos, K. Chander, A. Kriesch, R. Pala*, et al.*, "Nanoscale Conducting Oxide PlasMOStor," *Nano letters,* vol. 14, pp. 6463-6468, 2014.

[111] J. Aitchison, D. Hutchings, J. Kang, G. Stegeman, and A. Villeneuve, "The nonlinear optical properties of AlGaAs at the half band gap," *Quantum Electronics, IEEE Journal of,* vol. 33, pp. 341-348, 1997.

[112] J. A. Dionne, K. Diest, L. A. Sweatlock, and H. A. Atwater, "PlasMOStor: a metal− oxide− Si field effect plasmonic modulator," *Nano Letters,* vol. 9, pp. 897-902, 2009.

[113] S. Yu, X. Piao, D. R. Mason, S. In, and N. Park, "Spatiospectral separation of exceptional points in PT-symmetric optical potentials," *Physical Review A,* vol. 86, p. 031802, 2012.

[114] S. Yu, D. R. Mason, X. Piao, and N. Park, "Phase-dependent reversible nonreciprocity in complex metamolecules," *Physical Review B,* vol. 87, p. 125143, 2013.

[115] S. Yu, X. Piao, J. Hong, and N. Park, "Bloch-like wave dynamics in disordered potentials based on supersymmetry," *arXiv preprint arXiv:1501.02591,* 2015.

[116] X. Chen, H.-R. Park, M. Pelton, X. Piao, N. C. Lindquist, H. Im, *et al.*, "Atomic layer lithography of wafer-scale nanogap arrays for extreme confinement of electromagnetic waves," *Nature communications,* vol. 4, 2013.

[117] H. Kollmann, X. Piao, M. Esmann, S. F. Becker, D. Hou, C. Huynh, *et al.*, "Toward plasmonics with nanometer precision: nonlinear optics of helium-ion milled gold nanoantennas," *Nano letters,* vol. 14, pp. 4778-4784, 2014.

[118] M. S. Kumar, X. Piao, S. Koo, S. Yu, and N. Park, "Out of plane mode conversion and manipulation of Surface Plasmon Polariton waves," *Optics express,* vol. 18, pp. 8800-8805, 2010.

[119] S. Yu, X. Piao, K. Yoo, J. Shin, and N. Park, "One-Way Optical Transition based on Causality in Momentum Space," *arXiv preprint arXiv:1409.7031,* 2014.

[120] S. Yu, X. Piao, S. Koo, J. H. Shin, S. H. Lee, B. Min, *et al.*, "Mode junction photonics with a symmetry-breaking arrangement of mode-orthogonal heterostructures," *Optics express,* vol. 19, pp. 25500-25511, 2011.

[121] S. Yu, X. Piao, and N. Park, "Slow-light dispersion properties of multiatomic multiband coupled-resonator optical waveguides," *Physical Review A,* vol. 85, p. 023823, 2012.

초 록

양자 역학에서의 파노 공명은 비활성 기체의 여기 시 배위 상호작용을 다루기 위해 적용되어 왔으며, 파동의 간섭에 의해 얻어지는 일반적인 현상들 중 하나이다. 파노 공명의 주요 특징은 서로 다른 수명의 공진들 간의 간섭에 의해 발생하는 가파르고 비대칭적인 스펙트럼이다. 이러한 흥미로운 주파수 특성의 활용을 위하여, 양자 역학에서의 파노 공명을 광학적으로 모사한 다양한 파노 공명 구조가 플라즈모닉 나노 입자 및 메타 물질 기반에서 제안 및 연구된 바 있다. 박사 연구 기간 동안 본 연구자는 광학 및 플라즈모닉스 분야에서, 칩 상의 플라즈모닉 소자 및 광학적 스핀의 여기를 위한 파노 공명의 이용에 관한 연구를 진행해왔다. 본 졸업 논문에서는 파노 공명 구조의 비대칭적 주파수 특성을 플라즈모닉 스터브 구조 및 광학적 키랄 시스템에서 살펴보고자 한다.

이론 부분에서는 우선 초기의 양자 섭동 기반 해석, 고전 공진에 의한 해석, 그리고 간단하고 일반적으로 적용 가능한 결합 공진 방식과 같은, 파노 공명 현상의 이론적 기술 방식의 다양한 접근에 대해 다룬다. 또한 결합 공진 방식을 통해 파노 공명 현상의 정량화에 있어서 중요한 파노 비대칭 변수를 정의한다.

수치적 및 해석적 연구를 통해서는 플라즈모닉 금속-유전체-금속 도파로 스터브 구조에서의 파노 비대칭의 조절을 통한 플라즈모닉 센서를 제안한다. 또한 플라즈모닉 유도 투과 현상을 이용하여 매우 효율적인 플라즈모닉 칩 변조기를 소개하고자 한다. 제안된 변조기에서는 플라즈모닉 금속-유전체-금속 스터브 쌍에서의 파노 공명을 이용하여, 12dB 투과 대비 및 60% 수준의 투과율과 같은 우수한 특성이 확인되었다. 또한 스핀 나선성에 의한 파노 비대칭성을 이용하여, 에르미트 매질 변수를 갖는 보존적, 비자기적 매질에서 빛의 스핀을 여기하는 새로운 방식을 제안한다. 제안된 설계에서의 순수한 스핀 여기 정도 및 매우 민감한 주파수 특성을 이용하여, 실험적으로 접근 가능한 광학적 스핀 스위칭 현상 역시 소개한다.

.

주요어: 파노 공명, 광학, 플라즈모닉 시스템, 광학적 키랄 시스템.
학 번: 2008-23515